FIBEROPTIC SENSORS

Numerous parameters of light guided by optical fibers or transmitted by optical devices may depend strongly on the external environment. In some applications, this dependence is not welcome, as with fiber-optic telecommunications systems, where, for instance, attention is typically directed to avoiding bend- or stress-induced attenuation in optical cables. In other applications, however, this process may purposely be amplified, usually to make a specific light parameter selectively sensitive to a chosen environmental measurand. When optical fibers are used either to transmit the modulated light signals or to modulate some parameters of these signals directly via a specific physical phenomenon, the process is known as *fiber-optic sensing* (FOS) and the corresponding devices are known as *fiber-optic sensors.*

The need for fiber-optic sensors in the broad area of engineering is now widely accepted, especially in those applications where the benefits offered by this still novel technology are already more significant to the users than the higher costs of fiber-optic instrumentation in comparison with other sensor systems. One such application area is monitoring of civil engineering structures, including highway and railway bridges, dams, tunnels, large buildings, and underground mines. Such structures must resist environmental and in-service loads due to winds, earthquakes, traffic, thermal effects, construction, or environmental damage. For safety and maintenance their response must be carefully monitored. This information is needed to assess their overall "health" and to increase engineering knowledge for future projects. Pressure and strain gauges, stress cells, extensometers, accelerometers, and tiltmeters are among the variety of electrical and nonelectrical transducers that can be directly embedded in concrete, earth, rock, borehole or tunnel lining to sense and monitor structural loads and responses. None are well suited, however, to more demanding environments. Nonelectrical hydraulic devices are costly in labor-intensive inspection, maintenance, and repairs; they are difficult to multiplex and impossible to use for dynamic measurements. Electrical measuring devices are out of the question in open-air structures (risk of lightning) and in mining environments (risk of explosion). For these and similar applications, fiber-optic sensor technology offers strong potential for significant metrological improvement: electrical passivity, high bandwidth, safety in corrosive or explosive environments, immunity to electromagnetic interference, high sensitivity, miniature dimensions, possibility of remote operation, and direct compatibility with increasingly common fiber-optic data transmission and communication networks.

BASIC PRINCIPLES

A fiber-optic sensor is a device capable of converting a given, variable physical quantity into a modulated optical signal and then decoding it as a normalized electrical signal. For measurement purposes, this output signal is usually calibrated against a primary standard of the physical quantity of interest. The sensor then becomes a true secondary measuring instrument of this quantity. Figure 1 shows a schematic view of a basic fiber-optic sensor, where the sensing element S can be an optical fiber or another external optical element.

Definition

The sensing element S of the optical fiber sensor shown in Fig. 1 can best be formally described by the propagation ma-

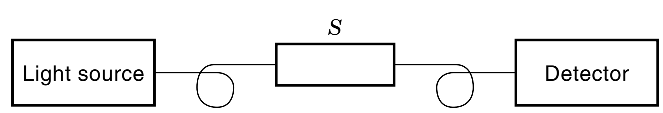

Figure 1. Basic configuration of a fiber-optic sensor; S denotes a sensing element.

J. Webster (ed.), *Wiley Encyclopedia of Electrical and Electronics Engineering*. Copyright © 1999 John Wiley & Sons, Inc.

trix $M(\boldsymbol{V}, \lambda)$ which normally depends on the physical environment represented by the vector $\boldsymbol{V}$ (depending on every imaginable external parameter) and on the spectral properties of the transmission medium (λ is the wavelength of propagating light beam). We may then describe the action of the sensor using the following equation:

$$\boldsymbol{E}^{\mathrm{M}}(\lambda) = M(\boldsymbol{V}, \lambda)\boldsymbol{E}(\lambda) \tag{1}$$

where $\boldsymbol{E}(\lambda)$ is the wavelength-dependent input electrical field entering the sensor, and $\boldsymbol{E}^{\mathrm{M}}(\lambda)$ is the measurand-modulated output electrical field exiting the sensor. By applying appropriate optical and electronic signal processing we can then recover M, $\boldsymbol{V}$, and finally those components of $\boldsymbol{V}$ that depend on the specific quantity we intend to measure. It is worth noting that $M(\boldsymbol{V}, \lambda)$ can conveniently be represented by a product of three separate factors as

$$M(\boldsymbol{V}, \lambda) = T \exp(i\phi_{\mathrm{m}}) B \tag{2}$$

Each of the three factors on the right side of the above equation is both environmentally sensitive and dispersive (dependent on the wavelength of transmitted light). The first factor, T, is the scalar transmittance, the parameter ϕ_{m} is the mean phase retardance, and finally B is the birefringence matrix characterizing the sensing element.

Classification

One of the most straightforward classifications of fiber-optic sensors can be derived directly from Eq. (2): *intensity sensors* are those where the measurand-modulated parameter is the scalar transmittance T, and consequently the intensity of transmitted light; *interferometric sensors* are those based on phase modulation; and, finally, *polarimetric sensors* are devices based on birefringence modulation. Both phase and birefringence effects may be recovered using interferometry or polarimetry, depending on specific application. This of course is a somewhat simplified approach; in reality all those parameters may be simultaneously affected, but one type of modulation usually predominates.

Fiber-optic sensors are often classified according to the nature of the sensing element: in *intrinsic* sensors, this element is an optical fiber, and the light is never permitted to exit the fiber into free space; in *extrinsic* sensors , it is a completely different optical part, and consequently in these hybrid structures the fibers are used exclusively for light-guiding purposes. In addition to standard sensors designed to measure a given parameter in one particular location only, we often mention *multipoint* or *multiplexed sensors,* which make it possible to take measurements in several different locations. Finally, it is worth noting that no other classical sensor systems have the same capability as fiber-optic systems to serve as truly *distributed sensors* and to enable the simultaneous detection not only of the magnitude of the modulating factor but also of the precise location of its occurrence and even of its spatial distribution.

Depending on the type of propagation occurring in the optical fibers, it is customary to differentiate between *single-mode* and *multimode sensors.* Depending on the degree of temporal coherence of the light sources involved, we can categorize sensors as *high-coherence, low-coherence,* or *incoherent.* In the rest of the paper, we will rely primarily on the notions introduced above, although many other less important approaches to classifying fiber-optic sensors, such as those based on the particular technology or on the application area, can be found in Ref. 1.

FIBER-OPTIC SENSOR COMPONENTS

Many FOS systems are based on standard commercially available components developed primarily for applications in optical fiber telecommunications. However, specifically designed and/or modified optical and fiber elements are also in use, since they can significantly improve the sensitivity and selectivity of the sensor and the stability of the system. Some examples of the components most often used in optical fiber sensing systems are described below.

Optical Fibers

Different types of FOS require different optical fibers for the transmitting, sensing, and receiving waveguides of the measuring system. For *extrinsic intensity* FOS, standard cylindrical fibers are normally used. The light signal can be intensity-enhanced when large-core multimode fibers or fiber bundles are applied for light-guiding purposes. A similar situation occurs with the fibers used to lead in and lead out the light in *intrinsic intensity* sensors. Specially prepared optical fibers such as doped fibers; hollow-core fibers filled with metal, liquid, gas or liquid crystals; and fibers with partially removed cladding or D-shaped cladding are often used as sensing elements. Since the lasing properties of erbium-doped fibers depend on various external parameters (such as temperature, stress, pressure, etc.), these fibers also can be used as sensing parts of the FOS despite the fact that they were developed originally for applications in optical fiber lasers and amplifiers.

For *polarimetric* and *interferometric* FOS, the methods of signal detection usually require a well-defined state and degree of polarization of the guided light. Therefore, optical fibers designed for these applications should have well-defined birefringence. In ideal cylindrical fibers [using the description of linearly polarized (LP) modes], the fundamental LP_{01} optical mode contains two degenerated orthogonally polarized modes propagating at the same phase velocity. In real fibers, both these modes have randomly different phase velocities, causing fluctuations of the polarization state of the light guided in the fiber. In highly birefringent (HB) fibers (2), the phase velocities for the two orthogonal light polarizations are high enough to avoid coupling between these two modes. Hence, if only one mode is excited, then the polarization of light guided in the fiber is preserved. On the other hand, if both modes in highly birefringent fibers are excited, then the polarization state of the light varies along the propagation distance. The state of the polarization depends on the phase difference $\Delta\phi$ between the two orthogonal linearly polarized modes. Since both these modes "see" the different refractive indices n_x and n_y, the phase difference between them changes at the distance z according to the formula

$$\Delta\phi = \frac{2\pi}{\lambda}\Delta n \cdot z \tag{3}$$

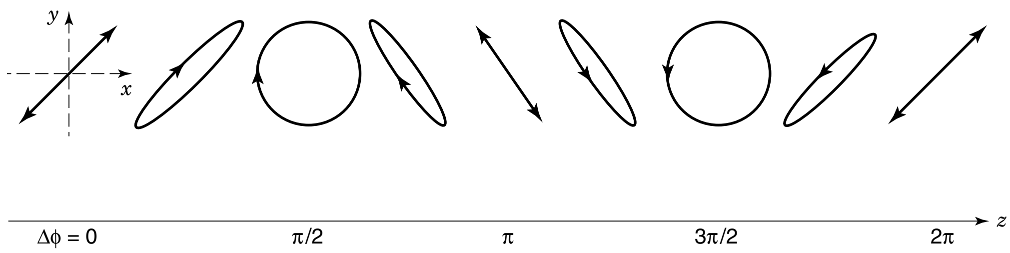

Figure 2. Evolution of the polarization states along the propagation axis in a HB fiber; input polarization is linear at 45° to the principal birefringence axes.

where $\Delta n = n_y - n_x$. Figure 2 shows the changes in the polarization states corresponding to the phase difference and to the propagation distance. These changes are periodical, with the spatial period defined as the beat length L_B:

$$L_B = \frac{\lambda}{\Delta n} \tag{4}$$

The birefringence of the fiber expressed by Δn is strongly influenced by external forces, and consequently the state of the polarization at the output fiber also depends on the local birefringence changes. This transduction mechanism is utilized in *polarimetric* sensors and will be explained later. High birefringence in optical fibers can be obtained by designing a core and/or cladding with noncircular geometry, or by using optically anisotropic core or cladding material (with intrinsic or induced anisotropy). Several cross sections of typical highly birefringent optical fibers are presented in Fig. 3. While in standard optical fibers the average beat length varies from 0.1 m to 1 m, in highly birefringent fibers it is only a few millimeters. Table 1 shows typical beat lengths at wavelength λ = 830 nm for commercially available highly birefringent fibers.

Other types of specialty fiber are low-birefringence (LB) fibers with birefringence lower than in standard optical fibers, and circularly birefringent fibers. Both of these fiber types are applied in sensors for magnetic field or electrical current measurements, where the magnetic field modifies the circular birefringence (Faraday effect). Another specialty fiber, recently introduced to the market by 3M, is the so-called polarizing fiber, which at a specific wavelength has a significantly different attenuation for two orthogonally polarized modes. After nonpolarized light is launched into 2 m to 3 m of such fiber, only the light in the low-loss polarized mode is transmitted and the mode with orthogonal polarization is completely attenuated (an extinction ratio of 1 : 1000 can easily be obtained). This type of fiber is designed with an absorbing metal layer placed close to the fiber core, or as a bent birefringent fiber. The polarizing effect is observed in a specific wavelength region only. Typical spectral characteristics of the attenuation in polarizing fibers are presented in Fig. 4.

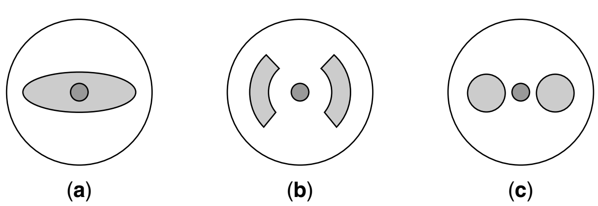

Figure 3. Cross sections of three HB fibers: (a) elliptical, (b) bowtie (stress-induced), (c) side-hole (stress-induced).

Optical Sources and Detectors

In almost every FOS application, semiconductor devices are used as sources and detectors. Other sources and detectors are occasionally used in specialized FOS for which the required parameters of light are not yet available from semiconductor sources (as in the case of sensors measuring luminescence with short-wavelength light sources).

The chosen light source for a specific sensor configuration should have the required stable output power, as well as the required light wavelength and coherence, which is especially important for polarimetric and interferometric systems. The coherence of the light source is described by the spectral linewidth $\Delta\lambda$ or equivalently by the coherence length $L_c = \lambda^2/\Delta\lambda$. The coherence length L_c is the maximal difference of optical path length at which the light can interfere. When the light is divided into two different beams propagating in different fibers then these two beams can interfere according to the phase difference

$$\Delta\phi = \frac{2\pi}{\lambda}(n_1 L_1 - n_2 L_2) \tag{5}$$

where $L_{1(2)}$ is the length and $n_{1(2)}$ is the effective refractive index of the fibers. The interference can be observed only if the phase difference $\Delta\phi$ is smaller than the phase change at the coherence length:

$$\Delta\phi < \frac{2\pi}{\lambda} L_c \tag{6}$$

Table 1.

Fiber Type	Beat Length L_B (mm)	Birefringence Δn (10^{-3})
Andrew E-type	5.08	0.16
Andrew D-type	4.71	0.18
Corning	2.99	0.28
Fibercore bowtie	2.10	0.39

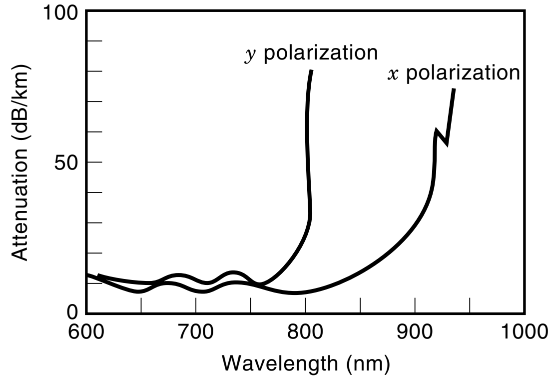

Figure 4. Spectral characteristics of the attenuation of two perpendicularly polarized eigenmodes propagated by a polarizing fiber. This fiber should be operated at about 830 nm for best performance.

Similarly, the state of polarization of the light propagating in a birefringent fiber can be defined only if the phase difference between the two orthogonal linearly polarized modes [Eq. (3)] meets the conditions of Eq. (6). Otherwise, the light exiting at the fiber end is depolarized and polarization-based signal processing is clearly not possible.

The coherence length for semiconductor sources varies from micrometers for light-emitting diodes (LEDs) to a few meters for single-mode diode lasers (LDs). The typical coherence of multimode LDs is a few millimeters, while superluminescent diodes (SLDs) have a coherence length of the order of a few tens of micrometers. High coherence is not always required for interferometric and polarimetric measuring systems. Low-coherence light sources are often intentionally used in certain interferometric FOS to reduce signal errors due to the presence of unwanted interference fringes (as in optical fiber gyroscopes). Also, in coherence multiplexing techniques the coherence should be low enough to avoid interference between the different measuring points. Therefore SLDs or edge-emitting light-emitting diodes are typically used in these systems. Recently even erbium-doped fiber lasers (with high-power 980 nm or 1480 nm LD pumps) began finding application in this area due to the facility of their coupling with other fibers. They are used as superluminescent fiber sources in interferometric systems (3) or fiber-optic amplifiers in FOS networks (4).

The important requirements of optical detectors used in FOS are bandwidth, noise, and dynamic range. The bandwidth determines the detector response time, which can be very long for low-cost discrete sensors but for certain types of distributed sensors and for time-domain multiplexed sensor systems should be very short. Typically, single detectors such as *pin* photodiodes, avalanche photodiodes, and photoconductors are still often used, but fast charge-coupled detector (CCD) lines and matrices are seeing greater use due to their increasing availability. The spatial light distribution or changes in it registered by the CCDs can be directly decoded as a measured quantity or may be further processed in demultiplexing techniques for distributed FOS.

Optical Fiber Components

Such elements as beamsplitters, wavelength filters, wavelength analyzers, polarization controllers, polarizers, phase and intensity modulators, and amplifiers are frequently used in optical sensor systems for optical processing or delivering the light beam to a specific location. All these elements are increasingly manufactured in optical fiber technology (*all-fiber* components) rather than in bulk optics (5) in order to obtain more mechanical and thermal stability as well as to satisfy the typical requirement for low optical losses in sensing systems.

One of the most frequently used all-fiber components is the *directional coupler* (6), which plays the role of a wavelength-selective beamsplitter. A schematic drawing of the bidirectional coupler is presented in Fig. 5. The directional coupler consists of two optical fibers placed close enough to each other to allow tunneling of guided light between the two fiber cores. The input light intensity I_i is partially transferred to both outputs I_{o1} and I_{o2}. For two identical lossless fibers, the energy transfer between them is described by the formulas

$$\begin{aligned} I_{o1} &= I_i \cos^2 \kappa L \\ I_{o2} &= I_i \sin^2 \kappa L \end{aligned} \tag{7}$$

where L is the effective coupler length. For parallel fibers, L is simply the length of the coupling region; for curved fibers with a bend radius R, it is given by $L = (\pi R/\gamma)^{1/2}$. The coupling coefficient κ is estimated in terms of coupled mode theory as an integral over the coupler cross section:

$$\kappa = \frac{\pi}{\lambda n} \int (n_c^2 - n_{cl}^2) e_1 e_2 \, dS \tag{8}$$

where n is the effective refractive index, $e_{1,2}$ are the normalized field envelopes of the guided modes in the fibers, and n_c and n_{cl} are the refractive indices of the fiber core and the surrounding cladding. In the simplest approximated form, coupling coefficient κ depends on the fiber's core separation distance h as follows:

$$\kappa = \frac{\lambda}{2\pi n} \frac{\nu^2 - \gamma^2}{a^2 \nu^2} \frac{K_0(\gamma h)}{K_1^2(\gamma a)} \tag{9}$$

where $\nu = 2\pi(n_c^2 - n_{cl}^2)^{1/2}/\lambda$, $\gamma = 2\pi(n^2 - n_{cl}^2)^{1/2}/\lambda$, a is the fiber core radius, and K_0 and K_1 are modified Bessel functions. For large core separations $\gamma h \gg 1$, the coupling coefficient is proportional to $\sqrt{\pi/2\gamma h}\, e^{-\gamma h}$.

Note that the energy transfer between the two fibers depends on the length of the directional coupler, on the distance between the fibers, and on the wavelength of the light. This

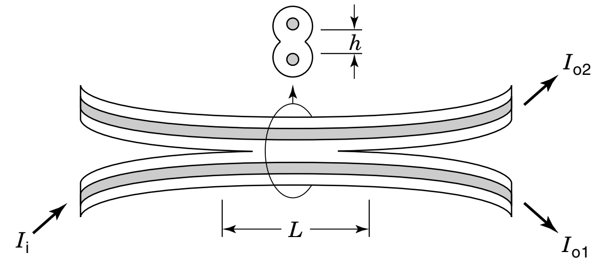

Figure 5. Schematic view of a bidirectional fiber coupler and its cross-section. I_i is input light intensity, I_{o1} and I_{o2} are output light intensities.

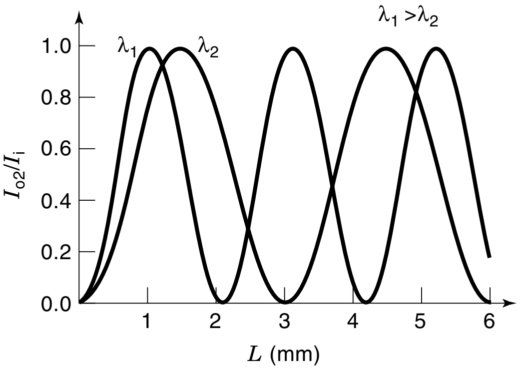

Figure 6. Power transmission ratio for a bidirectional coupler as a function of its effective length at two different wavelengths of light.

fact allows for convenient design of a directional coupler with the required transmission at the given wavelength. Figure 6 shows that by choosing the effective length of the directional coupler it is possible to obtain almost any power transmission ratio for two different wavelengths. Therefore the directional coupler can play the role of a bidirectional beamsplitter, a wavelength filter, or a wavelength-division multiplexer/demultiplexer. Directional couplers are most often made by polishing the fibers close to the core, by thermal fusion of two fibers, or by chemical etching. Polarization-maintaining couplers using highly birefringent fibers are also manufactured for specific applications. Figure 7 shows three examples of coupler use in fiber-optic sensor systems.

Fiber polarization controllers are often needed in sensing systems dealing with polarized light. The polarization controller transforms any given state of polarization into another state that is required in the particular application. This can be done either by modifying the fiber birefringence or by changing the birefringence axis. The first method is applied in controllers based on electromagnetic squeezing of the fiber. The external stress induces proportional birefringence change in a fiber. Therefore the controlled squeezing produces a required value of birefringence in the fiber and consequently the required phase shift between two perpendicular polarizations. The state of polarization has two degrees of freedom, and therefore two such squeezers rotated in relation to one another at a 45° angle are required for polarization controller.

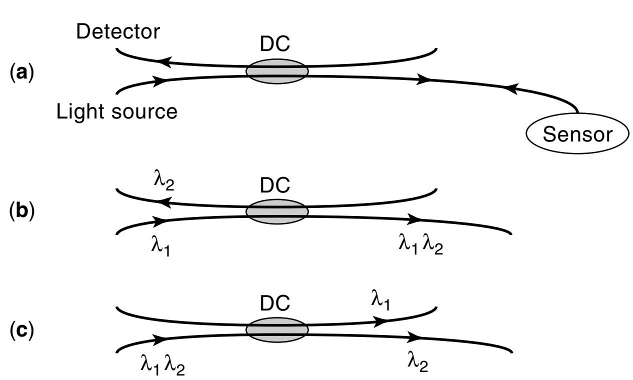

Figure 7. Three examples of possible applications of fiber directional couplers (DC) in fiber-optic sensor systems: (a) as a beamsplitter, (b) as a wavelength multiplexer, (c) as a wavelength demultiplexer.

Another type of polarization controller is based on changes of the birefringence axis of two elements playing the roles of a $\lambda/4$ plate and a $\lambda/2$ plate (three $\lambda/4$ plates can also be used for this purpose). The $\lambda/4$ plate introduces a $\pi/2$ phase retardation between two orthogonally polarized waves, while the $\lambda/2$ plate introduces a π phase shift. In the simplest and the most commonly used configuration, both plates are designed as coiled fibers. In bent fibers, the stresses induce birefringence and selection of the appropriate radius of curvature can produce the required phase retardation. Both fiber coils can be rotated relative to the z axis. The desired state of polarization at the output is obtained by adjusting the angle between the coils. Optical polarizers rather than polarization controllers are required in systems with elements depending on the polarization state. In all-fiber systems, often the polarizing fibers play the role of such polarizers, the extinction ratio increasing with the fiber length. Fiber polarizers can also be manufactured as polished fibers with the metal layer attenuating one polarization.

Intensity modulators, phase modulators, and frequency shifters are fiber devices frequently used in sensor systems to improve the performance of their detecting systems. Fiber-optic phase modulators utilize the refractive index changes caused by stretching or squeezing the fiber, and polarization controllers based on electromagnetic squeezing can often be used for these purposes. Typically, the phase modulators are designed as devices using an optical fiber wrapped around a piezoelectric ring, which changes its dimensions, and consequently the fiber length, in response to externally applied voltage. The frequency shifters, on the other hand, are manufactured primarily in integrated optics technology. The integrated optical modulators most widely used are based on the electro-optical Pockels effect occurring in lithium niobate crystals in channel waveguides surrounded by electrical electrodes. The coupling between the integrated channel waveguide in lithium niobate and the external leading optical fibers is inevitably associated with additional losses in the optical system and constitutes an obvious drawback; an important advantage, however, of the integrated optical chip is that numerous other elements such as integrated polarizers, directional couplers, or polarization controllers can be simultaneously designed and manufactured on the chip.

FIBER-OPTIC SENSORS: OVERVIEW

In this section we consider a representative sample of the most recent and successful embodiments of fiber-optic sensing devices. This overview, however, is by no means exhaustive; researchers worldwide have studied and explored a large number of sensing concepts during the last 15 years. Books such as Refs. 7 and 8 are suggested for anyone wishing to study this subject in more detail.

One focus of early fiber-optic sensor research was periodic measurands, but this work often ignored the issues of stability, repeatability, and temperature drifts and has not led to many practical installations. For this review, we have focused on practicability and on the potential for real implementations, which lead to an emphasis on absolute and quasistatic techniques. A significant majority of the conventional electrical and hydraulic measurement techniques that fiber-optic sensing technology is trying to outperform are in fact absolute

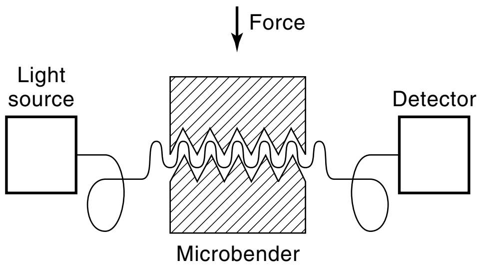

Figure 8. Basic microbending fiber-optic force sensor.

and quasistatic, with countless applications including industrial process control as well as stress analysis in civil engineering and geotechnics.

Intensity Sensors

Fiber-optic sensors based on intensity modulation are the simplest sensors, but they are often very successful and cost-effective devices. They can be developed using any kind of optical fiber, and noncoherent sources and simple detector units are usually adequate as other components of these systems. Most research effort in the area of intensity sensors has focused on overcoming one major drawback: finding a reliable referencing technique to compensate for a variety of analog signal instabilities. These instabilities include intensity and wavelength fluctuations of the light source and uncontrolled changes in detector responsivity as well as environmentally sensitive losses in optical fibers, couplers, and connectors.

Loss-Based Fiber-Optic Sensors. In bent optical fibers, higher-order modes tend to leak to the cladding when the bending radius decreases. This effect can be purposely amplified by applying a periodic microbending structure on an optical fiber, with the degree of induced attenuation depending upon the action of the parameter to be measured. If the bending is periodic with the bend pitch p, that is

$$p = C\pi rn(\mathrm{NA})^{-1} \tag{10}$$

where NA is the numerical aperture of the fiber, n is the refraction index of the fiber core, r is the core radius, and C is an index profile factor, then (9) the resonance condition can be achieved when the attenuation is maximum. Figure 8 shows a typical structure of a microbending force sensor using multimode fiber: in such a device, an external perturbation increases the bending of the fiber and causes progressive coupling of light energy into the radiation modes leaking out of it.

Based on this principle, many practical embodiments of the microbending sensor have been studied and developed. A good and timely review by Berthold (10) gives a complete analysis of this technology. One successful microbending sensor developed just recently (11) uses a multimode fiber as a sensing element and single-mode fiber as a lead-in. Such a configuration makes it possible to reduce noise significantly and to use more coherent sources; more importantly, it allows for a sixfold increase in sensitivity over microbending sensors built entirely of multimode fiber.

Like other intensity-based sensors, microbenders are sensitive to the optical power level in the system, and a large amount of research has been devoted to finding adequate referencing techniques to alleviate the problem. This has not been fully successful, since the possible origins of power fluctuations in the optical system are numerous and varied. Changes in output of the optical source, changes in transmission and bending loss along the fiber links, changes in coupling between optical connectors and other optical elements external to the sensor, and finally changes in the modal filtering properties of system components can all be responsible for these perturbations.

One successful self-referencing method, based on time-division normalization, was introduced by Spillman and Lord (12). The method is based on a 2×2 coupler and on introducing a specific time delay between the signals reflected back from the sensing and referencing arms and arriving back at the coupler. The ratio of the two signals is relatively independent of external perturbation sources, provided the time delay is short. Another similar method based on wavelength normalization utilizes a broadband source with two narrow spectral channels, dedicated to the reference and to the sensor signal, respectively (10).

The reported applications of microbending sensors include measurement of pressure (13,14) and temperature (15), as well as acceleration (16), strain (17), and speed (18). The main advantage of microbenders is their relatively high dynamic range of about 40 dB; the reported sensitivities go up to 10^{-10} m/Hz$^{1/2}$ (10).

Evanescent Sensors. An interesting, quite simple, and surprisingly effective group of sensors is based on the phenomenon of frustrated total internal reflection, where light energy is extracted from the propagating beam in the form of an evanescent wave. This extraction occurs in a predesigned location (a fiber element stripped of cladding or a separate optical element put in contact with a surrounding medium with a higher, or measurand-dependent, index of refraction).

Figure 9 shows a liquid-level sensor developed by Raatikainen et al. (19), where light delivered via a multimode input fiber undergoes two consecutive total internal reflections while passing through a sensing tip and then returns to the detection electronics via a multimode output fiber. When the sensing tip hits a liquid, the conditions for total internal reflection no longer exist and the output signal is attenuated at the level of 10 dB due to the evanescence of higher-order modes.

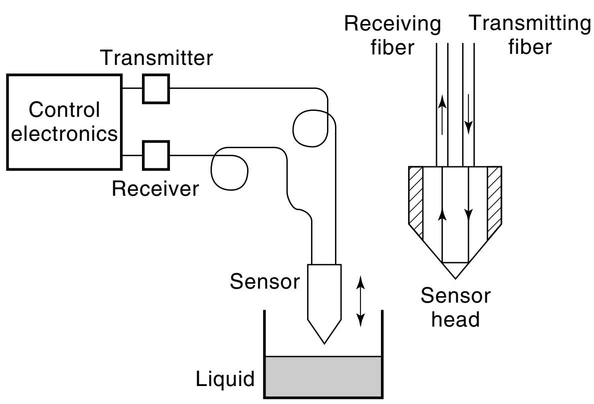

Figure 9. Schematic view of a fiber-optic liquid-level sensor. The magnification shows the light path within the sensor tip.

A more advanced configuration of a digital level transducer has been recently developed by Betta et al. (20). It is based on an optical fiber extended over the whole depth of a tank, with the optical cladding removed in 40 zones 0.5 mm long and with 25 mm of spacing between them. Each time the liquid level reaches or leaves one of those zones, the change in output power and the direction of this change are registered, giving information sufficient to determine the absolute value of the liquid level. A prototype with 1 m range and 25 mm resolution was manufactured and tested. It displayed no hysteresis, good repeatability, and accuracy of 25 mm.

Absorption Sensors. It is well known that the energy band structure in some semiconductor materials, especially in gallium arsenide (GaAs), depends strongly on the parameters of the external environment. Several successful approaches to the design of fiber-optic temperature and pressure sensors (21) rely on this effect, and some of them have already been commercialized (22).

The working principle behind this type of sensor is the displacement of the wavelength transmission limit in a GaAs crystal induced by pressure and/or temperature change. Pure GaAs crystal is transparent to infrared radiation and opaque to visible light; the optical absorption edge at 300 K and atmospheric pressure is 867 nm. Assuming isotropic compressibility of the crystal, a pressure change at constant temperature causes a change in the bandgap described by the following coefficient:

$$\gamma_p = \frac{dE_\Gamma}{dp} = 11 \times 10^{-5}\,\mathrm{eV/MPa} \tag{11}$$

The energy bandgap in GaAs will broaden with pressure, contrary to the conventional wisdom that all materials should become “more metallic” under pressure. Broadening of the bandgap will result in a displacement of the optical absorption edge illustrated in Fig. 10 and following the equation

$$\frac{d\lambda}{dp} = -0.0667\,\mathrm{nm/MPa} \tag{12}$$

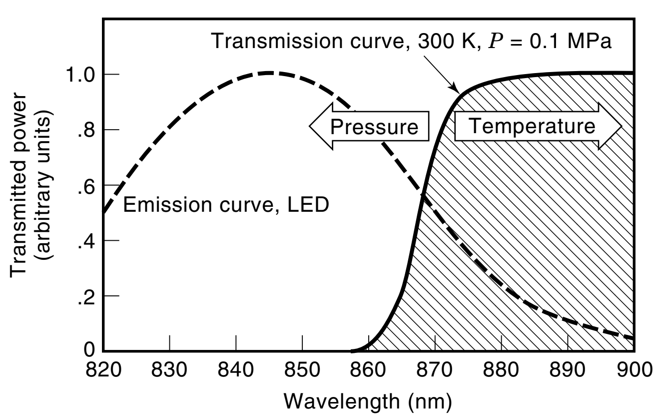

Figure 10. Transmission curve of GaAs and its dependence on temperature and pressure. The emission spectrum of the light source (dashed line) has to be carefully chosen to assure proper sensor operation.

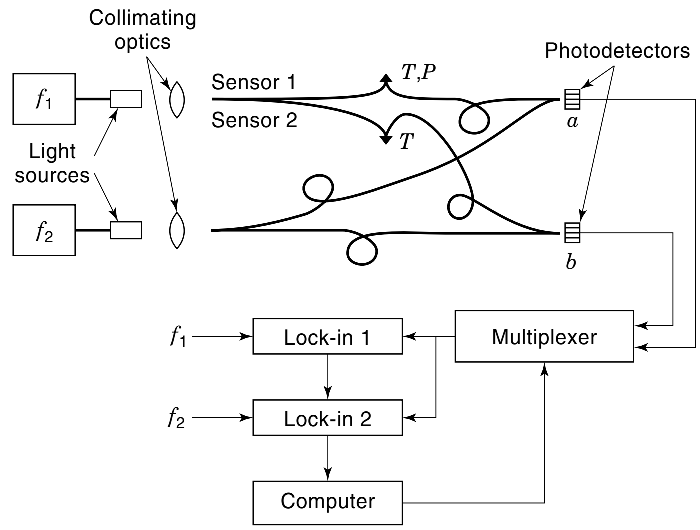

Figure 11. Compensation setup of a GaAs pressure sensor in two-source configuration.

The negative value of $d\lambda/dp$ indicates that the band edge will move toward shorter wavelengths with increasing pressure. Similarly, the GaAs energy bandgap will narrow with increasing temperature with the coefficient

$$\gamma_T = \frac{d\mathrm{E}_\Gamma}{dT} = -4 \times 10^{-4}\,\mathrm{eV/K} \tag{13}$$

which corresponds to a positive shift of the optical absorption edge at a rate of 0.28 nm/K.

The emission spectrum of the LED light source used with the sensor should overlap on both sides of the optical absorption edge. The displacement of this edge induced by temperature or by pressure changes modifies the fraction of light that falls into the absorption band, meaning that the transmitted intensity will change. A successful temperature sensor system based on this principle is presently manufactured by Nortech Fibronic Inc. (Canada) and allows a 32-channel measurement of temperature in range from −200° to 250°C. The maximum length of the optical cable between a sensing probe terminated with a semiconductor tip and the processing unit is 1 km (22).

Another configuration has been used to develop a pressure sensor based on the same principle (21), with special attention paid to compensation of the temperature artifact and to amplification of the pressure effects. If we assume that pressure and temperature effects on a sensor are factorizable, the output signal at a detector will be proportional to the intensity of the source multiplied by the factors related to temperature and pressure:

$$I(p,T) = I_o f(T) g(p) \tag{14}$$

Figure 11 shows a two-source compensation setup of a GaAs pressure sensor developed using this assumption and following the suggestion by Culshaw et al. (23). Two separate light sources supply light signals modulated at different frequencies f_1 and f_2. By using two reference arms in addition to two sensor arms, the influence of different individual detector responsivities is eliminated. It can be shown that the ratio of

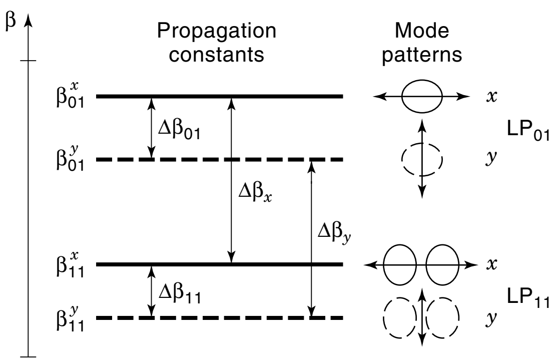

Figure 12. Propagation constants and mode patterns in HB bimodal fibers. Arrows indicate different possibilities of interference and show the corresponding phase shifts.

two signals registered at two detectors a and b is described by

$$\frac{I_a}{I_b} = g(p) \tag{15}$$

and depends directly on the pressure factor, assuming the light entering the two fibers is of equal intensity, with other effects canceled out. This assumption of equal intensity is problematic due to the fluctuations in ambient temperature and due to laser mode hopping resulting in uncontrollable deviations of compensation; however, equal intensity can be achieved by separately adjusting the coupling of light into each of the fibers. The output signal of the thermally compensated pressure sensor (21) clearly illustrates the benefits of the presented configuration. Good compensation has been achieved, especially at the lower range of temperatures from 5° to 25°C: in the worst case, the temperature error was reduced by more than an order of magnitude to less than 0.15 MPa/K. Further improvement can be achieved by controlled doping of the semiconductor material and by digital processing of the temperature-calibrated sensor signal.

Polarimetric Sensors

Polarimetric sensors may function in a single-mode or in a few-mode regime of propagation. Depending on the selected regime of operation, the different propagation constants shown in Fig. 12 have to be considered in order to understand the behavior of a specific sensor (24). Single-mode operation occurs when only one spatial mode LP_{01} or LP_{11} is excited at the fiber's input. No intermodal interference is observed in this case, as the second mode is absent.

Single-Mode Operation. If quasimonochromatic light linearly polarized at an angle φ with respect to the fiber's x axis is launched into the fiber and an analyzer turned to an angle α is placed at the output of the fiber, then the optical intensity detected will be

$$I = \tfrac{1}{2}(1 + \cos 2\alpha \cos 2\varphi + |\gamma| \sin 2\alpha \sin 2\varphi \cos \Phi_0) \tag{16}$$

where $\Phi_0 = \Delta\beta_{01} L$ is the phase. When external perturbations are introduced, they cause changes in the phase $\Phi_0 = \Delta\beta_{01} L$ of the fundamental LP_{01} mode (or correspondingly $\Phi_1 = \Delta\beta_{11} L$ for the LP_{11}). These will lead to a cosine variation of the observed intensity I measured after the analyzer, a variation that is in fact a polarization interference. The setup is then a *polarimetric sensor.* The interfering waves in this case are the LP_{01}^x and the LP_{01}^y polarization modes. With $|\gamma|$ we represent the correlation function between the polarization modes. This is a function of the product of the length L of the fiber, its polarization dispersion $\delta\tau$, and the spectral half-width $\delta\lambda$ of the source. The visibility V of the observed polarimetric response is

$$V = \frac{I_+ - I_-}{I_+ + I_-} = |\gamma| \frac{\sin 2\alpha \sin 2\varphi}{1 + \cos 2\alpha \cos 2\varphi} \tag{17}$$

An input polarizer (if the light is not linearly polarized) acts as a splitter, and the analyzer acts as a recombiner. If we define $k_1 = \sin^2 \varphi$ and $k_2 = \sin^2 \alpha$ as the power coupling coefficients of the splitter and the recombiner, then the expression for visibility becomes

$$V = |\gamma| \frac{4\sqrt{k_1 k_2 (1-k_1)(1-k_2)}}{1 + (1-2k_1^2)(1-2k_2^2)} \tag{18}$$

This expression is analogous to the well-known formula for visibility in classical two-beam interferometry (8). So maximum visibility is obtained if $k_1 = k_2 = 0.5$, that is, for $\varphi = \alpha = 45°$. In other words, maximum visibility occurs when the LP_{01}^x and LP_{01}^y polarization modes are equally excited by launching $\pm 45°$ linearly polarized light. In this case, the observed intensity and the visibility become

$$I = \tfrac{1}{2}(1 + |\gamma| \cos \Phi_0) \qquad \text{with} \quad V = |\gamma| \tag{19}$$

Evidently, if a monochromatic source is used, $\delta\lambda = 0$ and then the visibility will be $|\gamma| = 1$.

Two-Mode Operation. For a two-mode regime of operation, a bimodal sensing fiber must be used and the interference between either x- or y-polarized LP_{01} and LP_{11} spatial modes is observed. By letting $\Phi_x = \Delta\beta_x L$ and $\Phi_y = \Delta\beta_y L$, the intensity observed at the output of the fiber excited with x- or y-polarized quasimonochromatic light can be obtained (25) as

$$\begin{aligned} I_x(x,y,z) &= \eta_0 f_0^2(x,y) + \eta_1 f_1^2(x,y) + 2\eta_{01} f_0(x,y) f_1(x,y) \cos \Phi_x \\ I_y(x,y,z) &= \eta_0 f_0^2(x,y) + \eta_1 f_1^2(x,y) + 2\eta_{01} f_0(x,y) f_1(x,y) \cos \Phi_y \end{aligned} \tag{20}$$

In the equations above, η_0 and η_1 are the relative optical powers carried by the spatial modes. Depending on the detection setup, different expressions for the visibility can be obtained. Assuming the Gaussian approximation (26), the distributions of the two modes are expressed as

$$\begin{gathered} f_0(x,y) = \frac{1}{\sqrt{\pi \omega_x \omega_y}} F(x,y), \qquad f_1(x,y) = \sqrt{\frac{2}{\pi \omega_x \omega_y}} \frac{x}{\omega_x} F(x,y) \\ F(x,y) = \exp\left[-\frac{1}{2} \left(\frac{x^2}{\omega_x^2} + \frac{y^2}{\omega_y^2} \right) \right] \end{gathered} \tag{21}$$

The following three important subcases can readily be outlined: visibility at a point (pixel), visibility when half the pat-

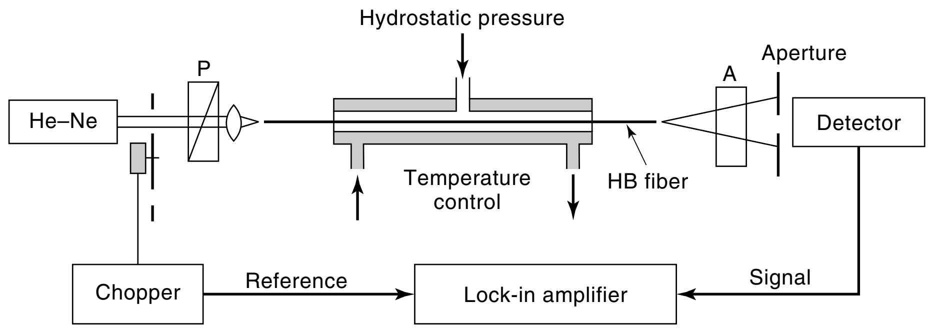

Figure 13. Basic configuration of a single-mode or bimodal polarimetric pressure sensor (A—analyzer, B—polarizer).

tern is detected, and visibility when an offset single-mode fiber is used. The visibility is then presented in the form $V(z, \eta_1) = |\Gamma_{x,y}|V_0$, where V_0 is a factor depending on the relative excitation coefficient of the second mode as well as on the detection scheme while $|\Gamma_{x,y}|$ are the correlation functions between the two interfering modes. In all of the cases, maximum visibility is obtained if the source is monochromatic and both modes are equally excited, that is, $\eta_0 = \eta_1 = 0.5$.

It is important to note that a fiber may be used simultaneously in the single- and the two-mode regime by operating it at two wavelengths at the same time. Thus *e*-core, D-shape, and bowtie fibers designed for single-mode operation at 850 nm (laser diode) will be bimodal when operated at a shorter wavelength of 633 nm or 670 nm, depending on the laser source. Alternatively, a polarimetric setup can be designed for 850 nm, and a polarization-sensitive intermodal interferometer for 633 nm. The setup illustrated in Fig. 13 could be utilized for this purpose. Note that the input and output polarization conditions in the single- and two-mode regimes are different. If the fiber is operated at both wavelengths and all possible polarizations, then three independent cosine responses can be obtained.

Differential Phase Shifts. When an external perturbation such as pressure, strain, or temperature is applied to a fiber of length L, it will change the phases $\Phi_i = \Delta\beta_i L$ $(i = 0, x, y)$ by the amount

$$\delta\Phi_i = \delta(\Delta\beta_i)L + \Delta\beta_i\,\delta L \tag{22}$$

If the external perturbation is hydrostatic pressure p, then an increase by δp will cause both $\Delta\beta_i$ and L to change by $\partial(\Delta\beta_i)/\partial p$ and $\partial L/\partial p$. So from Eq. (22) we can obtain

$$\frac{\delta\Phi_i}{\delta p} = \frac{\partial(\Delta\beta_i)}{\partial p}L + \Delta\beta_i\frac{\partial L}{\partial p} = \frac{2\pi}{T_{i,p}} = \Lambda_{i,p} \tag{23}$$

The above equation can also be rewritten as

$$\delta\Phi_i = \left(\frac{\partial(\Delta\beta_i)}{\partial p}\,L + \Delta\beta_i\,\frac{\partial L}{\partial p}\right)\delta p = \frac{2\pi}{\mathrm{T}_{i,p}}\delta p = \Lambda_{i,p}\,\delta p \tag{24}$$

Note that $T_{i,p}$ $(i = 0, x, y)$ has the dimensions of pressure, while $\Lambda_{i,p}$ has the inverse dimensions. These are experimentally measurable parameters and determine the sensitivity of the sensor to a given external perturbation [equations similar to Eq. (24) describe the phase changes induced by temperature or strain].

Polarimetric Pressure Sensor. The design of a practical high-hydrostatic-pressure polarimetric sensor with a predesigned sensitivity as expressed by the parameter $T_{i,p}$, is based on an important relation expressed simply as (24):

$$T_{i,p}L = C_i \cdot \lambda \tag{25}$$

where C_i is a constant. Thus, a longer fiber will exhibit greater sensitivity and vice versa. Note that if the source is not monochromatic, a longer fiber will produce a lower value of the correlation function $|\gamma|$, which in turn will null the cosine response of the sensor. Therefore, proper choice of the laser source is essential.

For pressure measurement (considering temperature to be a disturbing parameter), temperature- and pressure-induced phase shifts $\Delta\phi_S(p, t)$ will then be transformed into intensity changes $I_S(p, t) - I_0$ in accordance with the equation

$$I_S(p,t) = I_0[1 - \cos\,\Delta\phi_S(p,t)] \tag{26}$$

Figure 14 shows a topology of a polarimetric pressure sensor (PPS) in both reflection and transmission configurations, employing the principle of temperature self-compensation (27). The sensing (L_2) and compensating (L_1) parts of the sensor are assumed to be equal. The advantage of the reflection configuration is that only one fiber leadthrough is required to connect the sensor to the laser source and to the detection electronics. The advantage of the transmission version lies in the much higher level of optical signal, allowing for longer transmission distances and/or multiplexing of several sensing devices. The polarization axes of the sensing and the compensating fiber elements are rotated by 90°, while the input and output fibers are rotated at 45° relative to the sensing and compensating parts, respectively. Ideally, if equal sensing and compensating elements remain at the same temperature, their temperature-induced phase retardations will cancel out, and if they are placed under different pressures, the pressure-modulated output signal will be immune to temperature changes. In reality, however, if such an arrangement is to satisfy the requirements for an accurate pressure-measuring instrument, several important first- and second-order coefficients have to be considered to allow for simultaneous pressure and temperature effects on fiber birefringence. In a polarimetric cross-spliced sensor, the resulting unwanted sensitivity to temperature will still be present and can be de-

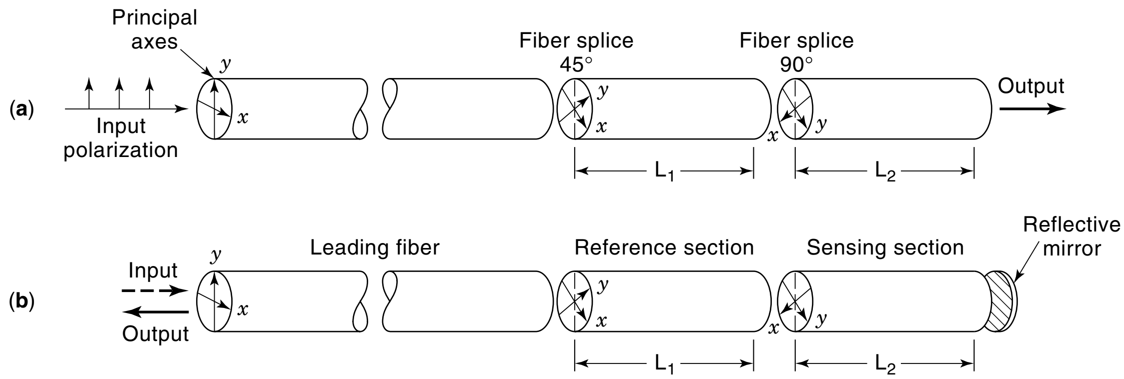

Figure 14. Temperature-compensated polarimetric fiber-optic sensor in (a) transmission and in (b) reflection configuration.

scribed by differentiation of the phase retardation with respect to temperature (28):

$$\rho_t = \frac{\partial \Delta\phi_{\mathrm{S}}}{\partial t} = \Delta L\, K_t + L K_{tp}\, \Delta p$$
$$K_t = \frac{1}{L}\frac{\partial \phi}{\partial \mathrm{t}}, \qquad K_{tp} = \frac{1}{L}\frac{\partial^2 \phi}{\partial t\, \partial p} \tag{27}$$

where $\Delta L = L_1 - L_2$, K_t is the first-order phase sensitivity to temperature, and K_{tp} is the temperature–pressure cross-sensitivity coefficient. This simple but informative equation provides important insight into designing a sensor with minimum temperature error. The first term in it can be minimized by choosing a small ΔL. The second term depends on fiber properties but will always be nonzero, and can only be minimized by carefully adjusting the fiber's technological and construction parameters.

Polarimetric Current Sensor. The need for fiber-optic sensing technology for high magnetic field and large current monitoring is now well documented. Conventional magnetic field and current sensor systems suffer from high susceptibility to electromagnetic interference, may lack the necessary bandwidth, are difficult to miniaturize, and cannot accommodate large numbers of measuring points at remote locations. Such monitoring can be especially valuable for protection, control, and fault detection in power plants, high-power transmission lines, substations, and distribution lines, where the high intrinsic electrical insulation of optical fibers is a significant advantage. Several techniques for fiber-optic magnetic field sensing have already been proposed (29), but only two approaches appear to be viable. The first is based on detection of a magnetic field by magnetostrictive effects, involving measuring the longitudinal strain produced in the optical fiber to which a magnetostrictive material has been bonded. The performance of such sensors is limited by the coupling efficiency of the magnetostrictive material and the optical fiber. Although various bonding and coating techniques have been explored, all usually lead to substantial hysteresis, temperature drift, and changes of fiber birefringence. The second approach is based on the well-known Faraday effect (30), consisting of a nonreciprocal circular birefringence induced in the propagation medium by a magnetic field and characterized by the Verdet constant V. The most convenient detection approach in this case is polarimetric sensing.

The Faraday effect may occur directly in standard or specifically doped optical fibers, but as V in silica fiber is very small, this type of sensor needs to be very long and as such will be prone to a variety of instabilities. For N turns of fiber around a conductor with a current I the Faraday rotation is given by

$$\Phi_{\mathrm{F}} = \int_{L_{\mathrm{F}}} V(\lambda, T)\, \boldsymbol{H} \cdot d\boldsymbol{L}_{\mathrm{F}} \tag{28}$$

where L_{F} is the propagation path and $\boldsymbol{H}$ is magnetic field. The material-dependent Verdet constant $V(\lambda, T)$ is dispersive and often varies strongly as a function of temperature. To assure successful operation of a sensor based on the fiber-sensitive element, it is extremely important to avoid intrinsic birefringence induced by core ellipticity or stress in the core–cladding area, and extrinsic birefringence induced by packaging and mounting. This parasitic effect can be alleviated to some extent by annealing the fibers at an elevated temperature (31). Figure 15 shows a simple polarimetric sensor based on this principle. Coils with 5 mm to 10 cm diameter and up to 300 turns have been produced, and a temperature sensitivity of 1.7×10^{-4} K^{-1} has been demonstrated over a $-20°$ to 120°C range. This technology has been transferred from NIST to the 3M Corporation for commercialization.

An approach based on extrinsic polarimetric sensors seems, however, to be more promising. The Faraday effect in ferrimagnetic garnets such as single-crystal yttrium iron garnets (YIG), Bi-doped YIG (BIG), and gallium-substituted YIG (Ga:YIG) (32,33) has been explored, since their Verdet con-

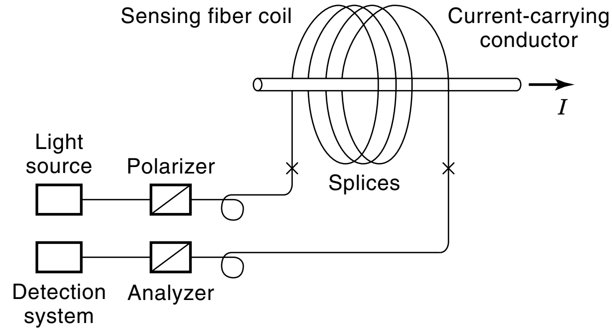

Figure 15. Polarimetric fiber-optic current sensor.

stant can be greater than that of silica fibers by a factor of several thousand. Although the large V gives such sensors an impressive advantage over the all-fiber configurations, inherent problems associated with the ferrimagnetic domain structure of these materials are large hysteresis, temperature drift of about 0.2%/K, nonlinearities, saturation at relatively low fields of about 0.1 T, and vanishing of response at frequencies of about 500 MHz. Recently, however, Inoue and Yamasawa (34) reported obtaining a Bi-doped garnet by liquid-phase epitaxy that shows a flat temperature characteristic from −10° to 80°C. Also, since the recent discovery of the large Faraday effect in $Cd_{1-x}Mn_xTe$ (CMT) (35), interest in this group of materials has been steadily growing with a view to their application not only in optoelectronic devices such as modulators and magneto-optic insulators, but also for polarimetric current sensors. These materials have improved thermal stability and can work at much higher fields (up to 25 T) and at higher frequencies (up to 5 GHz).

Interferometric Sensors

Fiber-optic interferometric sensors are usually designed following classical configurations of optical interferometers (8). In these devices, a range of physical measurands can induce modulation of phase in a sensing signal light beam, while the reference light beam remains unchanged. This phase change then has to be electronically processed, often by complex and sophisticated systems, to produce a useful intensity-type output signal from the interferometer proportional to the measurand. Although this technique offers very high sensitivity, it is extremely difficult to use outside the laboratory due to the unavoidable interference caused by environmental perturbations. One notable exception is low-coherence (or white-light) interferometry, which is presented later in more detail.

Classical Fiber Interferometers. Figure 16 shows the three best-known configurations of two-beam fiber-optic interferometers: (a) the reflective all-fiber Michelson interferometer, (b) the all-fiber Mach–Zehnder interferometer, and (c) a remote Fabry–Perot interferometer. Another configuration—the reciprocal Sagnac interferometer—is discussed separately. The

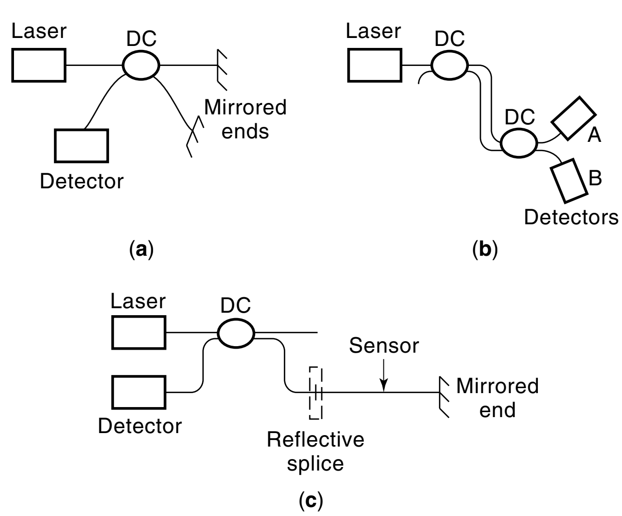

Figure 16. Three configurations of two-beam fiber interferometers: (a) Michelson, (b) Mach–Zehnder, (c) Fabry–Perot.

demodulation systems for interferometric sensors are usually based on *homodyne* detection, where the sensing and reference beams have the same frequency, or on *heterodyne* detection, where the reference beam has a fixed frequency that is different from that of the signal beam.

The all-fiber Michelson interferometer is based on a bidirectional single-mode fiber coupler that divides the input light beam from the laser source into two components—one propagated by the sensing arm, the other by the reference arm of the interferometer—and then combines the two reflected beams so that their interference can be registered by the photodetector. Assuming for simplicity that the polarization effects can be ignored, the electric fields propagating in the signal arm and in the reference arm can be treated as scalars and described as

$$E_S = E_{S0}\cos\left[\omega t + 2\left(\frac{2\pi L_S}{\lambda}\right)\right] \quad \text{and} \qquad E_R = E_{R0}\cos\left[\omega t + 2\left(\frac{2\pi L_R}{\lambda}\right)\right] \tag{29}$$

In this equation, E_{S0} and E_{R0} denote the amplitudes, λ is the wavelength of the light, and ω is its angular frequency. The phase difference will then be proportional to the path difference ΔL and can be expressed as follows:

$$\Delta\phi = \frac{4\pi}{\lambda}(L_S - L_R) \tag{30}$$

It may finally be shown that the irradiance at the detector is proportional to the absolute value of the squared sum of the superimposed electrical fields. The resulting formula is given by

$$I_d = I_0(1 - V\cos\Delta\phi) \tag{31}$$

(and corresponds to that of the polarimetric and dual mode sensors (Eq. (19)), where V is the visibility defined as in Eq. (17) and depending on both the reflectivity of the fiber ends and the coherence properties of the light source, but independent of the splitting ratio of the coupler. The maximum visibility occurs at the so-called quadrature condition when $\Delta\phi = \pi/2$ or when the path difference is equal to $\lambda/4$.

The Mach–Zehnder interferometer is based on two bidirectional fiber couplers, the first to divide the light beam into two components and the second to recombine the two beams exiting from the sensing arm and from the reference arm of the system. The sensitivity of this interferometer is only half that of the Michelson interferometer, as light propagates in each arm only once, and the phase difference is consequently described by

$$\Delta\phi = \frac{2\pi}{\lambda}(L_S - L_R) \tag{32}$$

The Mach–Zehnder configuration has, however, two significant advantages that more than compensate for the lower sensitivity. Two antiphase output signals from two photodetectors,

$$\begin{aligned} I_A &= I_0(1 - V\cos\Delta\phi) \\ I_B &= I_0(1 + V\cos\Delta\phi) \end{aligned} \tag{33}$$

can conveniently be used to provide a feedback loop for assuring operation at maximum sensitivity (quadrature condition when $\Delta\phi = \pi/2$). This configuration is also characterized by much lower backreflection into the laser diode, which assures the higher wavelength and power stability of the system.

A useful and more practical example of the multiple-beam technique is the fiber Fabry–Perot interferometer (FFPI). A resonant cavity of this device may be contained within the fiber, with semireflective splices (36), cleaved or mirrored (37) end faces, or Bragg gratings (38) serving as reflective surfaces. This cavity may also be external to the fiber, taking the form of an air gap between two cleaved fiber end faces, or between a fiber end face and a thin moving or deformable diaphragm (39). Following classical textbooks (40), the transfer function of an FFPI for the transmitted signal can be expressed by

$$I = \frac{I_0}{1 + F\sin^2(\phi/2)} \tag{34}$$

where F is a parameter describing the phase resolution and known as the *finesse* of the interferometer, and ϕ is the phase retardance after the light has passed through the cavity twice. When attenuation is disregarded, F may be described in terms of the mirror reflectance R:

$$F = \frac{4R}{(1-R)^2} \tag{35}$$

In the case of the frequently used low-finesse interferometer, the reflective surfaces may simply be the normally cleaved uncoated fiber ends, for which $R = 0.04$. The FFPI is then operated in a reflective configuration with visibility approaching 1 as the reflectivity is decreased. For $R \ll 1$ the FFPI signal may be approximated by the signal of the two-beam interferometer (Eq. (31)): $I_r = I_0\, 2R(1 - \cos\phi)$ for the reflective case and $I_t = I_0[1 - 2R(1 - \cos\phi)]$ for the transmitted signal.

Recently several quite interesting low-finesse Fabry–Perot-based fiber-optic sensors have been reported for a wide range of different measurands. Beard and Mills (41) developed an extrinsic optical fiber ultrasound sensor based on a thin transparent polymer film serving as the resonant cavity and mounted at an end face of a multimode fiber. The device can then be used for the detection and measurement of ultrasound with a sensitivity of about 60 mV/MPa. A phase-shifted extrinsic FFPI for dynamic strain measurements has been developed (42) using two laterally displaced single-mode fibers inserted into a hollow silica tube. Through an air gap these fibers face a multimode fiber acting as a reflector and forming a Fabry–Perot cavity. A high-sensitivity low-pressure sensor up to 13 kPa (100 Torr) has been developed (37) using a diaphragm bonded to the strained fiber containing the interferometer with two in-fiber mirrors, with the motion of the diaphragm producing a change in the length of a Fabry–Perot cavity. Even a fiber-optic sensor for electric field measurement has been developed around the concept of a low-coherence FFPI using a miniature cantilever beam, the deflection of which depends on the electrical charge induced by the external field to be measured (39).

For most of these sensors, however, active phase control and complex polarization control systems are usually required to keep them at their optimum operating points, at the expense of significant cost, high system complexity, and low potential for wide practical implementations. Recently Fürstenau and Schmidt (43) made a significant breakthrough in this area by proposing a two-wavelength passive quadrature demodulation system for FFPI vibration sensors, based on a low-coherence source in combination with adjustable interference filters and an electronic switching unit. This novel and cost-effective sensing system is now undergoing tests in an application for airport ground traffic monitoring.

White-Light Interferometry. Although low-coherence or white-light interferometry (WLI) has been known in fiber-optic sensing since the late 1980s (44), a significant research effort in this area became noticeable only around 1990. By then, the deficiencies of high-coherence classical interferometry, especially its inability to deal with absolute measurements and the enormous costs of the decoding equipment involved, were becoming more apparent. Since that time, significant advances in WLI sensor design, signal processing, and sensor multiplexing have been reported, and all prove that this technology has indeed matured to the point of becoming one of the most promising in fiber-optic sensing, thanks to its practicality and cost-effectiveness. Due to its youth, this technology has not yet received much book coverage, although several excellent reviews such as Ref. 45 have been devoted to this topic.

The principle of a WLI sensor system is illustrated in Fig. 17 in a reflective configuration. A broadband source, typically an SLD or a LD operated below threshold, launches light into a bidirectional coupler and into the sensing interferometer located in the measurand field. The modulated output signal of this interferometer is then coupled back through the coupler into the local receiving interferometer. When the optical path differences of the two interferometers are matched one to another within the coherence length of the white-light source, interference fringes with their amplitude modulated by the contrast function will be observed at the output of the receiving interferometer assuming a Gaussian spectral distribution of the source. The interferogram obtained at the photodetector can then be described (45) by

$$I = I_0\left\{1 + \tfrac{1}{2}\exp\left[-\left(\frac{2\,\Delta X}{L_c}\right)^2\right]\cos(k\,\Delta X)\right\} \tag{36}$$

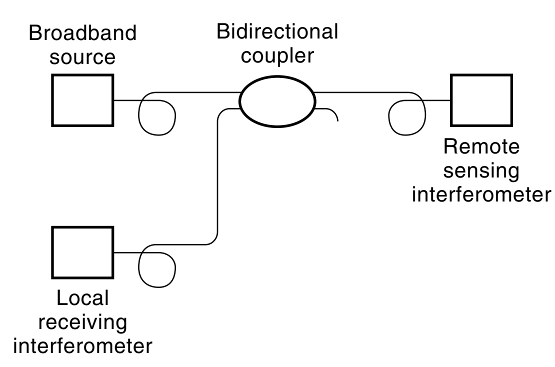

Figure 17. Basic configuration of a white-light interferometric fiber-optic sensor.

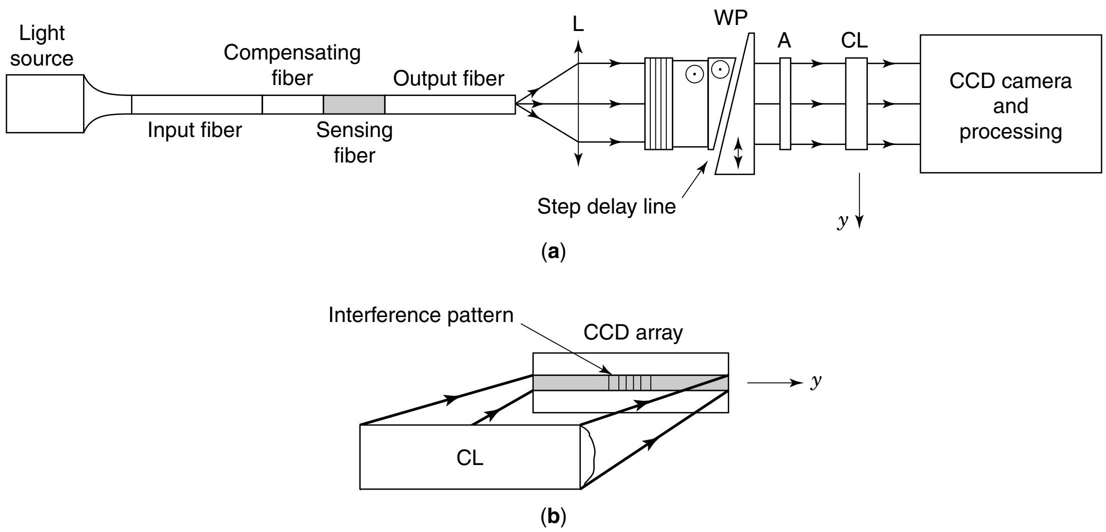

Figure 18. Electronically scanned white-light interferometric strain sensor in temperature-compensated configuration: (a) general setup, (b) detail of the output pattern exiting the receiving interferometer.

where L_c is the coherence length of the source, $\Delta X = X_1 - X_2$ is the mismatch between the optical path differences of the sensing and the receiving interferometers, k is the wave number, and I_0 is the total optical intensity arriving at the photodetector. Note that the necessary condition for the system to work is $\Delta X < L_c$. It is clearly evident that any change of the external measurand acting upon the sensing interferometer will result in the interference pattern being shifted. This shift can then be easily registered or compensated for at the receiving interferometer, giving an absolute measurement of the external parameter in question. Many application-specific sensor systems have been developed to measure temperature (46), strain (47), pressure (48), and force (49) using an often complex variety of signal-processing techniques (45). In recent years, processing based on electronic scanning for low-coherence sensing systems has attracted much attention, since it does not require any piezoelectric or mechanical scanning devices and makes the system more compact, more stable, and less expensive.

An example of an electronically scanned WLI strain sensor based on HB fibers and with a Wollaston prism serving as a receiving interferometer (50) is shown in Fig. 18. The light source is an SLD with a central wavelength $\lambda_0 = 820$ nm and a coherence length of about 15 μm. The input light is linearly polarized by the polarizer (or by a polarizing fiber) aligned at 45° to the polarization axes of the sensor in order to excite both polarization modes equally. The sensor itself is composed of two exactly equal lengths of the HB fiber spliced with their corresponding polarization axes rotated at 90° and giving a total phase shift at the output of the system close to zero. Light from the output of the sensor is collimated by lens L and passes through the Wollaston prism WP, which is made of crystalline quartz. The polarization axes at the output of the sensor are aligned to be parallel to the polarization axes of the WP. Therefore, the x- and y-polarized modes of the sensor are spatially separated by the Wollaston prism with the bisection angle α equal to 2°. The two modes interfere after passing through the analyzer A, which has its transmission azimuth aligned at 45° to polarization axes of WP. The cylindrical lens CL focuses the output beam on the CCD camera (or a CCD array) with a horizontal resolution of 1024 pixels, enabling registration of the resulting interference pattern with an adequate signal-to-noise ratio.

At an arbitrary point along the horizontal direction of the CCD camera, the two polarization modes intersect at an angle α, and the resulting intensity of the interference pattern may be written as

$$I(y) = I_0(y)[1 + \gamma(\phi_s + \phi_{WP})\cos(\phi_s + \phi_{WP})] \qquad (37)$$

where $I_0(y)$ is the bias intensity profile of the output beam; ϕ_s is the phase imbalance between the polarization modes at the output of the sensor; $\phi_{WP}(y)$ is the phase difference introduced by the Wollaston prism, which can be expressed as

$$\phi_{WP} = \frac{2\pi}{\lambda_0}\alpha(y - y_0) \qquad (38)$$

and γ is the coherence function of the light source. The longer wedge of the Wollaston prism may be shifted transversely across the beam, allowing for adjustment of the zero position of the interference pattern with respect to the scanning area of the CCD camera. The parameter y_0 in Eq. (38) indicates the position of the center of the longer wedge with respect to the edge of the scanning area. Assuming that the sensor is initially perfectly balanced, the phase shift occurring at the output due to the elongation of the sensing part of the fiber will be

$$\phi_s = L_0\left(\Delta\beta + \frac{\partial\Delta\beta}{\partial\epsilon}\right)\epsilon \qquad (39)$$

where L_0 is the initial length of the sensing part of the fiber and ϵ is the strain applied. An increase in the output phase

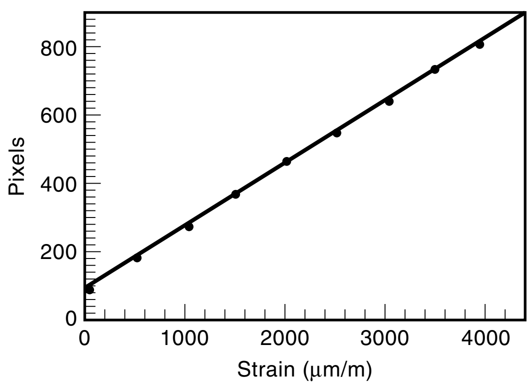

Figure 19. Example of output signal of the WLI strain sensor: position of the center of interference pattern versus strain.

shift ϕ_s results in a transverse shift Δy of the white-light interference pattern, proportional to the absolute value of ϵ:

$$\Delta y = \frac{\lambda_0 L_0}{2\pi\alpha}\left(\Delta\beta + \frac{\partial\Delta\beta}{\partial\epsilon}\right)\epsilon \tag{40}$$

Consequently, it is clear that processing of the signal digitized by the CCD camera needs to establish the location of the center of the white-light interference pattern determined by the symmetry axis of the coherence function $\gamma(.)$. This can be achieved in a three-step procedure as discussed in detail in Ref. 45. First, the bias intensity function is determined by simple numerical filtering-out of higher harmonics from the output intensity. Then, in the second step, the coherence function is determined, and finally, in the third step, the upper part of the coherence function is approximated by a parabolic function, the symmetry axis of which determines the central position of the white-light interference pattern. This position may thus depend on the action of the selected measurand. For instance, in the case of strain measurement illustrated by Fig. 19, an operating range of 4000×10^{-6} was achieved with an absolute accuracy of 0.5% of full scale (FS) (including temperature drift of 40°C) and a resolution of about 10^{-3} with no hysteresis effect. Similar performance has been achieved in pressure measurement up to 100 MPa with an almost identical configuration, the only difference being that the sensing element was subjected not to elongation but to hydrostatic pressure (51).

Bragg Grating Sensors

Periodic changes of the refractive index profile in optical waveguides are equivalent to gratings and constitute a source of scattering for the guided light. When the spatial period of such a grating is matched with the light wavelength, the scattered light can be guided as a backreflected wave. This phenomenon is applied for instance in distributed feedback resonators in semiconductor lasers, in distributed fiber Bragg reflector structures, and in sensing structures (52).

Assuming that the refractive index profile n_p in an optical fiber changes with the spatial period Λ as

$$n_p = n_0 + \Delta n \cos\left(\frac{2\pi}{\Lambda}z\right) \tag{41}$$

the complex amplitudes of the forward mode A and the backreflected mode B fulfill the coupled equations (53)

$$\begin{aligned} \frac{dA}{dz} &= -\mathrm{i}\kappa B \exp(2i\,\delta z) \\ \frac{dB}{dz} &= \mathrm{i}\kappa A \exp(-2i\,\delta z) \end{aligned} \tag{42}$$

A normalized frequency δ represents the mismatch between the wavelengthλ and the spatial period of the grating:

$$\delta = \frac{2\pi n}{\lambda} - \frac{\pi}{\Lambda} \tag{43}$$

where n is the effective refractive index of the guided wave. The coupling coefficient κ depends on the effective depth of the refractive index modulation:

$$\kappa = \frac{\pi}{\lambda n}\int 2n_0\,\Delta n\, e_1 e_2\, dS \tag{44}$$

where $e_{1,2}$ are the normalized electric field envelopes of the guided modes, and the integration is over the fiber cross section. Solution of Eq. (42) for a grating with length L gives the following expression for the reflectivity:

$$R = \frac{|B(z=0)|^2}{|A(z=0)|^2} = \frac{\kappa^2}{\gamma^2\coth^2\gamma \mathrm{L} + \delta^2} \tag{45}$$

where $\gamma^2 = \kappa^2 - \delta^2$. The reflectivity depends strongly on the length of the grating, and consequently the backreflection can be high even when the index of refraction has a small modulation amplitude Δn. The maximum reflection, as illustrated in Fig. 20, is obtained at a specific wavelength λ_B that is twice the period of the grating within the fiber:

$$\lambda_{\mathrm{B}} = 2n\Lambda \tag{46}$$

Bragg gratings also make it possible to couple two modes copropagating inside a multimode fiber core, or to couple core and cladding modes. This phenomenon occurs when Eqs. (43) and (46) are fulfilled with $2n$ replaced by the difference between the effective refractive indices of the two coupled modes, $n_1 - n_2$. In this case, the resonant Bragg wavelength λ_B corresponds to longer grating periods Λ. Typically the spa-

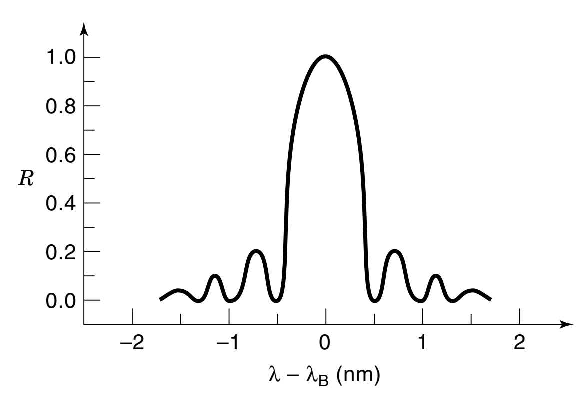

Figure 20. Theoretical dependence of the reflectivity in Bragg grating structures on wavelength ($\kappa = 1\ \mathrm{mm}^{-1}$, $L = 2$ mm, $\lambda_B = 1330$ nm).

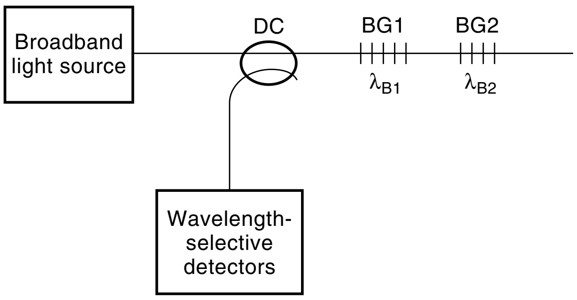

Figure 21. Basic configuration of a fiber Bragg grating sensor, with two Bragg gratings BG1 and BG2.

tial period Λ in such long periodic gratings is hundreds of micrometers long, while in reflecting fiber Bragg gratings a period of only hundreds of nanometers is typical.

Fiber Bragg gratings are manufactured by writing a permanent periodic modulation of a fiber's index of refraction within the fiber using a photoinduced effect. This effect is particularly useful in germanium-doped silica fibers. The resulting pattern of the refractive index is induced by the interference fringes generated by the interfering ultraviolet or near-ultraviolet radiation. The effect may be obtained using either a standing wave created by the light guided by the fiber, or the diffraction and interference of light externally illuminating the fiber.

The wavelength λ_B of the backreflected light depends strongly on temperature T, a fact that constitutes a major drawback of this method:

$$\frac{\partial \lambda_B}{\partial T} = 2\left(\Lambda \frac{\partial n}{\partial T} + n\frac{\partial \Lambda}{\partial T}\right) \tag{47}$$

Obviously this wavelength also depends (in a manner similar to that expressed in the above equation) on a variety of potential external measurands such as strain or pressure. Several complex techniques have been proposed (54), with very limited success, to solve this fundamental problem of discrimination between temperature effects and those induced by the measurand in question. Proposed solutions involve (1) using two gratings, one isolated from strain and playing the role of a reference grating; (2) using two gratings for different wavelengths; and (3) using two gratings for the same wavelengths, but with different strain sensitivities (e.g., formed in different fibers). Measured sensitivities of 10 pm/K, 1 pm/(μm/m), and 5 pm/MPa have been reported (55) to temperature, strain, and hydrostatic pressure, respectively. The difficulty of the measurement is increased by the requirement for high-precision wavelength measurement: λ_B may change by as little as 1 nm within the full scale of the intended measurement. The simplest FOS systems with fiber Bragg gratings use a broadband source to encompass the Bragg wavelength and a wavelength-selective detector to measure the reflected wave (Fig. 21). Using several different gratings with different λ_B, we can construct a quasidistributed sensor system with wavelength-division multiplexing techniques.

Fiber-Optic Gyro

Fiber-optic gyros (FOGs) are most mature of all fiber-optic sensors and are now widely considered in altitude and heading reference systems, and for car navigation systems with reduced requirements. A solid-state configuration gives them a significant advantage over conventional mechanical gyros based on the principle of inertia of spinning masses. FOGs have found practical application in aircraft, tactical missiles, trains, autonomously guided vehicles, and marine gyrocompasses (56).

The principle of operation of FOGs is based on the rotationally induced phase shift of the light propagating in the fiber coil (Sagnac effect) (8). When the fiber ring in Fig. 22 rotates in the inertial system, then light propagated in the same direction will traverse a longer path to return back to the initial point A (moved to A') at the ring. The additional path is equal to αR, where R is the ring radius and the angle $\alpha = \Omega\tau$ depends on the rotation rate Ω and the time τ it takes the light to traverse the ring. For a ring length L, the time τ is equal to Ln/c, where c/n is the light speed in a medium with the refractive index n. Consequently, the phase shift ϕ for a light wave with the angular frequency ω that traverses the rotating ring can be expressed as

$$\phi = \left(L + \Omega RL\,\frac{n}{c}\right)\omega\,\frac{n}{c} \tag{48}$$

Similarly, for a counterpropagating wave we obtain

$$\phi_c = \left(L - \Omega RL\,\frac{n}{c}\right)\omega\frac{n}{c} \tag{49}$$

A FOG operates by measuring the phase difference $\Delta\phi = \phi - \phi_c$ between two counterpropagating waves, the difference being proportional to the rotation rate Ω of the fiber coil:

$$\Delta\phi = \phi - \phi_c = 2\Omega RL\omega\left(\frac{n}{c}\right)^2 \tag{50}$$

Three principal passive configurations for a FOG are an interferometer (I-FOG) with an open loop, an I-FOG with a closed loop, and a resonator (R-FOG). In the I-FOG with the open loop (Fig. 23), light from the laser source is divided by a directional coupler into two beams with equal intensity counterpropagating in a fiber coil composed of many turns. Then the outcoming light is mixed again in the directional coupler and the interference of the two waves is measured by the de-

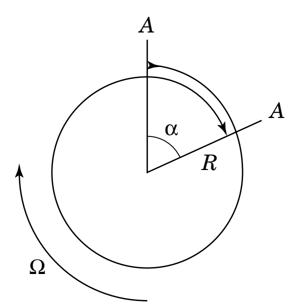

Figure 22. Sagnac effect in optical fiber ring.

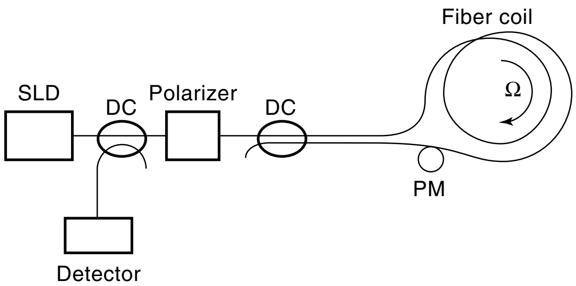

Figure 23. Basic configuration of an I-FOG with an open polarization-maintaining fiber loop. PM is a phase modulator.

tector. The interference, similarly to the Eq. (31) and (32) for two-beam interferometers, can be expressed as follows:

$$I = I_0(1 + V\cos\Delta\phi) \tag{51}$$

where V is the interferometric coefficient and I_0 is the input intensity modified by any losses in the optical system. To avoid parasitic dependence of interference on the polarization state, the configuration requires use of a polarizer, and the fiber in the coil has to be polarization-maintaining. The detection system can be improved by incorporating a phase modulator (PM) with a fixed frequency f_m at the end of the fiber loop. This induces an additional phase shift

$$\Delta\phi_m = \phi_m \cos(2\pi f_m(t+\tau)) - \phi_m \cos(2\pi f_m t) \approx F\cos(2\pi f_m t) \tag{52}$$

where ϕ_m is the modulation depth and $F = 2\phi_m \sin(\pi f_m \tau)$. In this case, the output signal at the detector can be expressed as follows:

$$I(t) = I_0\{1 + V\cos[\Delta\phi - F\sin(2\pi f_m t)]\} \tag{53}$$

Then the detected signal is modulated with an amplitude that depends on the magnitude of the rotation rate Ω, with the phase dependent on the direction of rotation.

The I-FOG with the open loop is the simplest configuration and the most popular to date. For applications that require higher performance and dynamic range, the I-FOG with the closed loop is more promising. In this configuration, a tunable frequency shifter is added at the fiber coil end. The frequency shifter changes the angular frequency of the first wave when it enters the fiber ring, and of the second wave when it exits the fiber ring. Therefore the phase shift of the first wave is modified in the optical fiber coil as follows:

$$\phi = \left(L + \Omega RL\frac{n}{c}\right)(\omega - \omega_s)\frac{n}{c} \tag{54}$$

where ω_s is the frequency shift induced by the frequency shifter, and the second counterpropagating wave has a phase shift given by Eq. (49). Then the phase difference $\Delta\phi$ is equal to

$$\Delta\phi = 2\Omega RL\omega\left(\frac{n}{c}\right)^2 - \mathrm{L}\omega_s\frac{n}{c} \tag{55}$$

Changing the frequency ω_s, one can null the phase-shift difference, and the obtained frequency ω_0 for $\Delta\phi = 0$ gives the rotation rate:

$$\omega_0 = 2\Omega R\omega\left(\frac{n}{c}\right) \tag{56}$$

The frequency shifter is typically made as an electro-optical modulator in integrated optics technology, mounted together with a Y junction, which plays the role of a beamsplitter (similar to a directional coupler), and with a polarizer. The closed-loop configuration gives a very good bias and stable scale factor (i.e., proportionality between the rotation rate and the output). In both types of I-FOG, low-coherence light sources (such as SLDs or erbium-doped fiber lasers) are used to minimize noise due to reflected and backscattered light. However, the use of low-coherence sources causes fluctuations due to the potential wavelength drift. The sensitivity of I-FOGs depends on the length of the polarization-maintaining fiber in the coil. Increasing the length of the fiber increases costs (polarization-maintaining fibers are expensive in comparison with other elements in FOGs) and also increases noise due to the variable temperature distribution. Some of the above problems can be solved by resonator FOGs.

In R-FOGs (Fig. 24), the phase shifts of the two counterpropagating waves are detected independently. The detector Det1 measures the interference between the light traversing the fiber ring and that incoming from the light source in the same direction. The frequency shifter FS1 changes the frequency to maximize the intensity measured by Det1. Similar processing occurs with the counterpropagating wave, and the difference between the frequencies shifted by FS1 and FS2 is directly decoded as a rotation rate. The R-FOG configuration requires highly coherent and stable sources of light, but the polarization-maintaining fiber loop is much shorter than in I-FOGs. R-FOG systems are still, however, in the research stage. Many other concepts, such as ring laser systems, Brillouin ring lasers, or the use of depolarized light in a fiber coil, could be applied in advanced FOG development. It should be noted that the fiber-optic ring resonators and coils could also be used as sensors for measuring other measurands than the rotation.

Distributed Sensors

Due to the unidimensional structure of an optical fiber, fiber-optic sensing technology offers the unique possibility to simul-

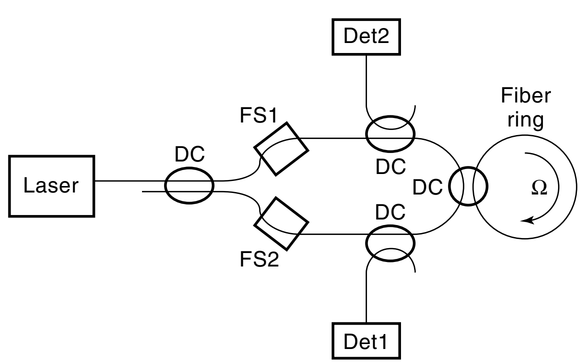

Figure 24. Basic configuration of the resonator-based gyro (R-FOG).

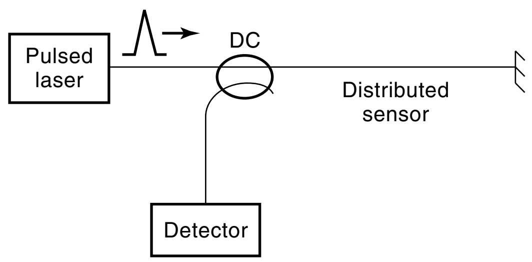

Figure 25. Principle of an OTDR-based distributed sensor.

taneously measure not only a given parameter but also its real-time spatial distribution. Distributed fiber sensors are intrinsic fiber-optic sensors that allow sensing of the variation of the measured quantity along the fiber as a continuous function of distance (57). They rely in principle on optical time-domain reflectometry, which is commonly used for diagnostics in fiber telecommunication systems.

Figure 25 shows the principle of operation of the optical time-domain reflectometer (OTDR). A high-power light pulse is launched into the sensing fiber and propagates with the group velocity v_g. The light is reflected at discontinuities and is scattered mainly in the elastic process of Rayleigh scattering, which is caused by the microscopic fluctuations of the refractive index in the fiber. The detector measures the time dependence of the backscattered light signal, and the time of the measurement t determines the distance $z = tv_g/2$ at which the light pulse was backscattered.

Figure 26 presents a sample of the return signal measured by the OTDR. Since the light is attenuated in accordance with an exponential law, the backscattered power P measured by the detector is calculated as (8)

$$P = P_0(1-\eta)\eta RD \exp(-2\int \alpha(z)\,dz) \tag{57}$$

where α is an attenuation coefficient, P_0 the initial pulse power, D the length of the pulse, R the backscattering reflection coefficient per unit length, and η the coupling ratio in the directional coupler. The slope of the logarithm of the detected power at constant reflection R is proportional to the attenuation:

$$\frac{d}{dt}\left(\log\frac{P}{P_0}\right) = -\alpha(z)v_g \tag{58}$$

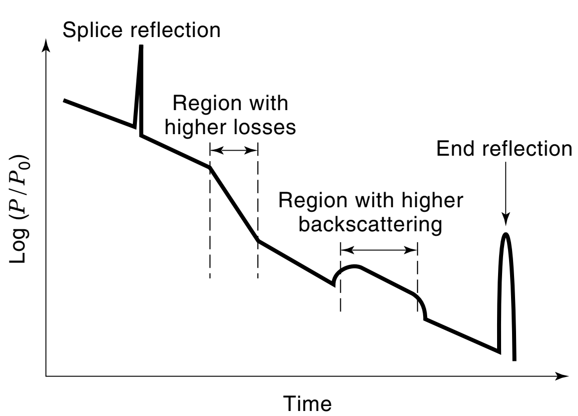

Figure 26. Sample of the detected signal from a distributed fiber-optic sensor.

Thus those parts of the fiber with higher losses are recognized as regions where the detected characteristic has a larger slope, and those parts with higher backscattering are recognized as regions where there is a higher value of detected power. Any discontinuities (e.g., splices or a fiber end) produce high reflections and jumps in the characteristic of the detected signal.

The OTDR sensors detect the changes of the backscattered reflections R or changes of the losses α induced by the measured quantity. The Rayleigh scattering coefficient depends on temperature, and it can be applied in a temperature sensor (58). Measuring the losses in OTDRs with specially prepared fibers makes it possible to detect the temperature, pressure, liquid leakage, displacements, and other mechanical and chemical measurands. Another possibility is measuring the state of polarization of the backscattered light. Such polarization OTDRs measure changes in birefringence of the fiber, which is sensitive to strain, pressure, magnetic field, electric field, and temperature (59).

Besides the elastic Rayleigh scattering, the inelastic processes of Raman and Brillouin scattering occur in optical fibers. Raman scattering is caused by the molecular vibrations, while Brillouin scattering results from bulk vibrations. Brillouin OTDRs (60,61) and Raman OTDRs have detectors analyzing the spectrum of backscattered light. The ratio of the Stokes and anti-Stokes peaks and the frequency shift in the spectrum can be a source for determining the temperature or strain.

The OTDR allows measurement of changes in the measurand with a spatial resolution approximately equal to 1 m. Another technique, optical-frequency domain reflectometry (OFDR), offers better resolution. It is based on a chirped radio-frequency-modulated light source and on determining the position of light backscattering via the measured frequency.

FIBER-OPTIC SENSOR SYSTEMS

In a simple one-sensor, one-fiber arrangement of a discrete fiber-optic sensor, the optical fiber is largely underutilized as a transmission medium, mostly because the capacity of one information channel is much greater than the information generated by a typical sensor output. Important gains can therefore be made by multiplexing the fiber link by tapping several sensing devices into one passive fiber highway to increase the maximal number of sensors and to establish data telemetry channels. Such a configuration will obviously decrease the installation costs per sensor and at the same time increase the attractiveness of fiber-optic sensing technology for many potential users. Furthermore, industry has a need to install increasing numbers of sensors in surveillance and automation systems in factories, chemical plants, mines, offshore platforms, aircraft, and spacecraft. Another driving force behind development of multiplexed fiber-optic sensor systems is their close relation to fiber-based LANs; the fact that they utilize the same or similar components will keep their prices low even if the market for industrial fiber-optic sensor systems is only in the early stages of emergence.

Basic Multiplexing Concepts

There are two principal multiplexing concepts that can be applied in designing a sensor system: In one class, a given num-

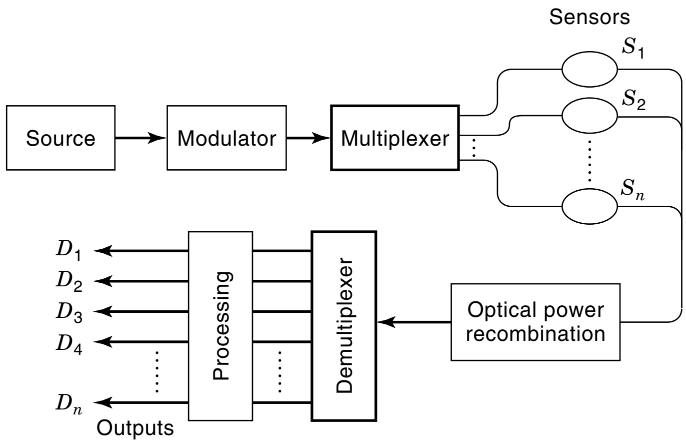

Figure 27. Generalized fiber-optic sensor network.

ber of sensors, having only one and the same property modulated by the external measurand field, can be incorporated into a single passive highway loop. Then some kind of multiplexing, addressing, and decoding is added to the system to allow monitoring, detection, and interpretation of a returning output signal from a given sensor at a particular location. A second class involves the so-called orthogonal modulation scheme, where one measurand modulates different optical properties of the sensor. Such a system is capable of simultaneously performing measurements of several different physical parameters.

With the variety of optical fiber sensors currently under development, it does not seem possible yet to characterize the multiplexed system most likely to emerge as the standard, although its topology and parameters will obviously depend upon the type of sensor used, and in almost any multiplexed system at least four basic functions will have to be performed: powering the system at a level adequate for the predesigned power budget of the network, addressing and interrogating (identifying) a sensing device at a chosen discrete location, detecting the measurand-modulated signal of a given sensor, and eventually evaluating and calibrating the acquired individual sensor signals. The topological arrangement of a network, the generalized form of which is shown in Fig. 27, will largely depend on the scheme chosen for sensor addressing and demodulation.

Some the best-known and most basic network topologies are linear array, ring, reflective/transmissive star, and ladder network. Both passive and active elements such as fiber links, splices, connectors, couplers, polarization controllers, light sources/detectors, modulators, multiplexers/demultiplexers, and sensors are themselves used to implement physical interconnections and components of a multiplexed optical fiber sensor network.

Examples of Discrete Sensor Multiplexing Techniques

Although many different multiplexing schemes and branching network concepts, often very sophisticated and costly, have been extensively investigated and reported (see for instance Refs. 62, 63, 64), industrial applications are usually looking for simpler, lower-key, and cheaper ideas. This short overview of multiplexing techniques starts with such an idea of a simple multiplexing configuration.

Space-Division Multiplexing. Space-division multiplexing (SDM), utilizing separate fiber paths and separate detector–source arrangements for individual sensors, is the easiest method to use and has been already implemented (65). Although it was initially dismissed as a low-key and inelegant approach, the rapidly decreasing prices of optoelectronic components (primarily laser sources and detectors) are imposing a reevaluation of the prospects for practical implementation of this method. The power budget of such a system is excellent, crosstalk is nonexistent, and the failure of one channel can usually be tolerated. The method can also be easily combined with a TDM or a WDM scheme (see the two following sub-sub-subsections) at the source–detector terminal unit. Several possible topologies of the SDM method involve common light source with multiple detector array, multiple sources with common detector, single source and single detector with one-to-N and N-to-one switching, and synchronous switching.

Wavelength-Division Multiplexing. The advantage of applying a wavelength-division multiplexing (WDM) scheme (see Fig. 28) for sensor arrays is that it still permits an excellent power budget for the system, as in the case of SDM, while affording savings in the form of a smaller number of necessary fiber links and connections. The light signal sent to each sensor is directed through the appropriate WDM coupling components, which are broadly similar to those designed for fiber communication systems. The most important problem related to this method is obtaining sufficient selectivity of the utilized wavelength division filters; to achieve this, several techniques can be employed, including the very promising spectral splicing technique with a broadband source and narrowband filters such as diffraction or holographic gratings. To further increase the number of multiplexable devices, the technique may obviously be used not only with single-, but also with dual- or multiple-fiber optical links.

An industrial differential-pressure transducer with wavelength-multiplexed power and data channels has been developed (66). It utilizes a resonant element optically excited at

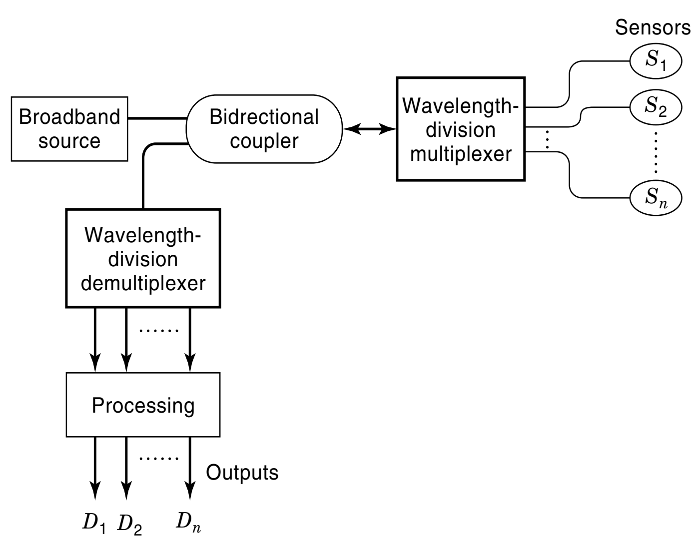

Figure 28. Wavelength-division-multiplexed fiber-optic sensor system.

one wavelength of 850 nm, the pressure-modulated frequency of which is read out at another wavelength of 633 nm using the same two-wavelength single-fiber link.

Another example of a WDM system involves a digital rotary- and absolute-angular-position sensor utilizing a reflective code plate with ten channels, providing a resolution of 0.35° (67). Two light-emitting diodes with overlapping spectra and a single micro-optic multiplexer–demultiplexer composed of a GRIN rod lens and a miniature grating are used to disperse the spectrum and recombine the spectral components from each channel after reflection by the code plate. This idea has been proposed for a fly-by-light control of the angular position of a throttle or a fuel control valve on an aircraft.

Time-Division Multiplexing. Time-division-multiplexed (TDM) systems usually require fast and costly electronics and because of this are less attractive for many industrial applications where the cost of installed hardware becomes a dominating factor. In a TDM system, each individual sensor signal can be identified and decoded at the detection end of the setup by arranging different propagation delays for the light signals returning from sensors at different locations. This method can also be coupled with the WDM technique in multiwavelength monitoring systems, with one wavelength affected by the measurand and another used for the reference (68). The method has several important advantages, including the large number of channels, the one-source, one-detector configuration, and equal applicability to both coherent and noncoherent systems. However, usually small optical path differences between the sensors require nontrivial processing. To this end, many complex topologies have already been proposed and reviewed (69). One possible form is a TDM optical passive sensor highway incorporating a commercially available electromechanical switch. Such a system has practically no crosstalk, but a stringent requirement to contain the time-sharing switching sequence within a very short period must be satisfied.

Frequency-Division Multiplexing. The general approach to frequency division multiplexing (FDM) of fiber-optic sensors is to send an amplitude- or frequency-modulated output signal from every sensor in a given network through an assigned frequency channel. The method consists of modulating several light sources by signals of different frequency, or modulating one light source with several frequencies (63) and then combining and separating signals at the detection end of the system employing a multichannel phase-sensitive (usually lock-in-based) detection scheme. One solution is a so-called matrix array method of FD multiplexing of intensity sensors, similar to the one developed by Mlodzianowski et al. (70) in a three-sensor configuration. It has much simpler and slower electronics than typical TDM systems, and has a good potential for industrial intensity-modulated sensor multiplexing.

Coherence Multiplexing. Theoretical analysis (71) indicates that numerous WLI sensors with different optical path differences might be interrogated in a serial system by scanning the receiving interferometer. To date, however, a practical realization of only a four-sensor system has been reported (72). There are several factors limiting the number of multiplexed sensors, such as the power budget, the degradation of the contrast of white-light interference (WLI) patterns with increasing number of multiplexed sensors, and the difficulties in proper choice and precise control of optical group imbalances of all sensors in the system in order to assure separation of the signal and noise interference patterns. Furthermore, in many practical applications all multiplexed sensors need to be temperature-compensated. A typical temperature-compensated sensor consists of two equal lengths of highly birefringent (HB) fiber spliced with the polarization axes rotated by 90°, so that its total group imbalance is close to nil (50). The requirement of temperature compensation conflicts with the principle of coherence multiplexing, which requires significantly different group imbalances between all multiplexed sensors.

Recently an interesting way of overcoming all these difficulties has been reported for sensors based on HB fibers (72). Such sensors are easy to manufacture, especially in that their group imbalances may be controlled simply by measuring the lengths of the fiber components. A system of four serially multiplexed sensors including two temperature-compensated pressure sensors and two temperature sensors has successfully been developed and tested. A modified concept of the temperature-compensated sensor has been adopted for hydrostatic-pressure measurements in order to simultaneously achieve the temperature desensitization of each pressure sensor while maintaining the possibility of individual addressing. The modified pressure sensor consists of three different fiber elements: sensing, compensating, and addressing fibers of lengths L_S, L_C, L_A, respectively. The sensor elements can be made of different types of HB fiber, but their lengths have to satisfy the following condition:

$$K_S^T L_S - K_A^T L_A - K_C^T L_C = 0 \tag{59}$$

where K_S^T, K_A^T and K_C^T are corresponding temperature sensitivities. By choosing the proper lengths and types of fiber for the particular sensor elements it is possible to fulfill the condition of Eq. (59) while setting the total group imbalance ΔR of the sensor at the desired value. In order to avoid overlapping of the noise and the signal interference patterns, the total group imbalance of every additional sensor connected to the serial system has to satisfy the following condition:

$$\Delta R_N = \sum_{i=1}^{N-1} (\Delta R_i + Q_i) \tag{60}$$

where ΔR_i and Q_i are the group imbalance and the operation range of the ith sensor, and the summation is carried out over all sensors already existing in the system.

Examples of Industrial Sensor Systems

As examples of practical implementations, we have selected several application-specific industrial sensor systems reported to have been recently installed in different environments. More information can be found in recent books (7,8) and conference proceedings (see for instance Refs. 54, 68).

Fiber-Optic Stress Monitoring. The fiber-optic stress cell (FOSC) has been developed as a safe and reliable method for embedding and interfacing the FOS (of pressure, load, or stress) in concrete, rock, or soil materials under harsh environmental conditions (73). This simple and practical method combines fiber optics with elements of traditional hydraulic measurement technology based on a compensation method in which stress in the material surrounding the pressure cell is compensated by automatically adjusted pneumatic or hydraulic pressure within it. The assembly of the fiber-optic stress cell is composed of a pressure pad connected to a fiber-optic pressure sensor. The pressure cell is optimized for stress measurements by adjusting the plate surface/thickness ratio to minimize both the measurement error and the influence of the different modulus of elasticity between the cell and the surrounding material. The cell is attached to a housing containing a fiber-optic polarimetric pressure sensor in a temperature-compensated configuration and equipped with two specially designed pressure leadthroughs to input and output the leading fibers. The connectorized optical leading cables are protected by resistant plastic tubes to withstand the effects of the grouting process during bore-hole installation. Thus, internal pressure induced inside the FOSC, dependent on the stress in the surrounding material, can be directly read out by the fiber-optic pressure sensor and relayed to the remote digital demodulation and measurement unit via long optical cables. A prototype of this device has been successfully installed for load monitoring in a salt mine near Braunschweig, Germany, which is now being used as a nuclear waste disposal site.

Fiber-Optic Thermal Monitoring. An eight-channel fiber-optic sensor network has been installed for thermal monitoring of the stator of a 900 MW turbogenerator (65) by the Bertin Company in France. The system is based on white-light interferometry and uses optical phase demodulation provided by a dual-wavelength passive scheme in a polarimetric configuration (74). The temperature sensor itself is a miniature calcite probe aligned between two polarizers. The eight-channel system is achieved through space-division multiplexing using one LED source at 830 nm per sensor and a common optical and electronic demodulation unit. This unit sequentially interrogates the sensors at a rate of 13 Hz via an 80 m eight-fiber bundle cable and reconstructs the temperatures from the demodulated signals. The accuracy of the system is reported as 0.5°C in the operating range of 20°C to 120°C with accidental rises up to 200°C. The installation is located in the EDF nuclear power plant of Trickastin 1 and is proving successful for high-accuracy temperature monitoring in a harsh environment (high temperature, humidity 93% at 70°C, vibrations at 10 Hz to 100 Hz, and accelerations of 2*g*).

Fiber-Optic Combustion Monitoring. Real-time pressure measurements on internal combustion engines can provide information for optimum control of engine speed, throttle, air/fuel ratio, and exhaust gas recirculation. Optrand Inc. (USA) is now marketing an intensity-modulated fiber-optic diaphragm sensor integrated within a spark plug, where cylinder pressure flexes the diaphragm and modulates the light reflected from it and coupled back into the input fiber (75). This fiber is metal-coated and temperature-resistant, allowing it to be integrated with the sensor housing and providing a necessary hermetic seal. The sensor is powered from a LED source through a fiber-optic coupler, and the diaphragm is laser-welded to the sensor body. The operating range of this sensor is up to about 7 MPa (1000 psi) with overpressure up to 21 MPa. The range of temperatures is −40° to 550°C, and the frequency range is 0.1 kHz to 15 kHz. The overall accuracy of this system is reported to be better than 5%.

Fiber-Optic Damage Detection Monitoring. Fiber-optic submarine communication cables are exposed to a variety of damage risks from anchoring or fishing equipment. Early detection of such incipient damage can significantly improve the reliability of undersea transmission installations. To satisfy this requirement, a prototype 66 kV XLPE fiber-optic communication cable containing an integrated fiber-optic mechanical damage detection sensor has been developed in Japan and is now used in real installations (76). The detection part contains four single-mode fibers placed in shallow grooves in the outside part of the cable every 90°. When lateral force is applied to the cable, some of the monitoring fibers become laterally compressed and their transmission losses greatly increase. Monitoring of these losses by the OTDR system means that the increasing risk of damage to the cable can be detected long before any degradation of the actual optical transmission becomes visible, and corrective action can be undertaken in time to save the cable. The system is able to detect cable deformation rates from 10%, whereas the deterioration of communications is normally noticed only at 40% cable deformation.

Fiber-Optic Traffic Monitoring. A fiber-optic airport ground traffic surveillance system has been installed in the Braunschweig airport in Germany to detect and identify vehicles or aircraft movement via monitoring of structural vibrations (77). The system is based on a fiber-optic extrinsic Fabry–Perot microinterferometer cantilever-beam-type vibration sensor. The Fabry–Perot cavity is formed by the air gap between the end of the sensing fiber and a low-reflectivity mirror, and its length depends on the vibrations. The sensing element is powered from a low-coherence SLD at $\lambda = 1300$ nm via a bidirectional coupler. The reflected modulated signal returns through the same coupler and is split into two components before entering a two-wavelength passive quadrature demodulation unit, which converts the two phase-shifted interference signals into output voltages. The sensors are located at taxiway intersections with runways and cemented at the edge of the taxiways without damaging the pavement. Each sensor is connected to the system via one of eight connectorized single-mode optical fibers inside a common optical cable about 1 km long running to the control unit. The reported system has now been in continuous operation for more than two years and has proven successful under all weather conditions.

Fiber-Optic Navigation Monitoring. The fiber-optic gyro (FOG), discussed earlier, is an open-loop ring interferometric rotation sensor and is the first mass-produced FOS for applications in vehicle, missile, or aircraft navigational systems (78). The system is manufactured by Hitachi and is currently installed, among other applications, in luxury automobiles. The sensor is entirely composed of polarization-maintaining fiber, uses an SLD source, and has a CMOS-integrated high-precision signal-processing system based on DSPs. The accuracy of rotation measurement can be as high as 0.01°/h and is stable within a temperature range from −30° to 80°C. The system is mass-produced at a maximum rate of 5,000 units per month and can be used for automotive navigation in planned intelligent transportation systems to overcome heavy traffic congestion or in other applications such as attitude control systems or direction measuring systems.

Fiber-Optic Displacement Monitoring. A WLI system of fiber-optic displacement sensors for monitoring the integrity of civil structures (SOFO) has been developed and implemented in Switzerland (79). It is based on a double all-fiber reflective Michelson interferometer in tandem configuration (80), with the sensing fiber pretensioned and coupled to the measured structure and with a free temperature-compensation fiber. The system is powered by an SLD at 1300 nm, and one arm of the analyzing Michelson interferometer is terminated by a mobile mirror. The sensor length may vary from 20 cm to 50 m, and the resolution is 2 μm; the dynamic range for measuring elongation is 1%. The sensors can be connected serially in chains by coherence multiplexing. It has been recently reported that this system has already been installed on four bridges and in several tunnels and dams, with a total of 600 sensors being installed since 1993 (79).

Fiber-Optic Current Monitoring. Commercial optical current transformers based on Faraday rotation in Bi-substituted rare earth iron garnet (BiRIG) materials have been developed by Panasonic in Japan (81) for metering in electric power systems. The optical magnetic field sensor head itself can take the form of a confocal sensor or a miniature fiber-integrated sensor. The polarizer, analyzer, and leading fibers are integrated together within the sensor head, and the intensity-modulated signal is acquired in a polarimetric configuration. It has been reported that the appropriate combination of garnet composition and optical design can yield 1% of sensor accuracy within a temperature range from -20°C to 80°C, with an ac linearity of 1% for input current up to 300 A.

FUTURE OF FIBER-OPTIC SENSORS

During the last 15 years, extensive research has been done on every imaginable fiber-optic sensing mechanism (3), making it rather difficult to come up with an entirely novel and exciting sensing idea. Many of the ideas studied, however, remain mere ideas, with no chance of practical implementation in a real environment. A promising trend is now developing in that more and more research groups are taking approaches that are application-oriented, and consequently such implementation issues as packaging, interconnecting, and above all reliability and multiplexing of fiber-optic sensors and systems are becoming the focus of attention. Research on FOS technology for industrial applications is still, however, in the early stages of development.

Three important aspects have to be addressed simultaneously in the near future for wider successful commercialization of these systems in direct competition with traditional sensing systems. These aspects are: (1) developing accurate, reliable, and cost-effective sensor systems; (2) safe packaging and interfacing of sensors with their working environment; (3) optical multiplexing, signal processing, and remote data telemetering for the installed sensor arrays. Research in these directions will certainly continue to increase, since the technology remains genuinely attractive in many application areas.

BIBLIOGRAPHY

1. G. Cancellieri (ed.), *Single-Mode Optical Fiber Measurement: Characterization and Sensing,* Boston: Artech House, 1993.
2. J. Noda, K. Okamoto, and Y. Sasaki, Polarization-maintaining fibers and their applications, *J. Lightwave Technol.,* **4**: 1071–1089, 1986.
3. P. F. Wysocki et al., Characteristics of erbium-doped superfluorescent fiber sources for interferometric sensor applications, *J. Lightwave Technol.,* **12**: 550–567, 1994.
4. J. Saether and K. Blotekjaer, Noise performance of multiplexed fiber-optic sensor systems with optical amplifiers, *Opt. Rev.,* **4**: 138–144, 1997.
5. C. Tsao, *Optical Fibre Waveguide Analysis,* Oxford: Oxford Univ. Press, 1992.
6. M .J. F. Digonnet and H. J. Shaw, Analysis of a tunable single mode optical fiber coupler, *IEEE J. Quantum Electron.,* **QE-18**: 746–754, 1982.
7. B. Culshaw and J. Dakin (eds.), *Optical Fiber Sensors,* Norwood, MA: Artech House, 1989, Vols. 1, 2.
8. E. Udd (ed.), *Fiber Optic Sensors—An Introduction for Engineers and Scientists,* New York: Wiley, 1991.
9. D. C. Marvin and N. A. Ives, Wide-range fiber-optic strain sensor, *Appl. Opt.,* **23**: 4212–4217, 1984.
10. J. W. Berthold, Historical review of microbend fiber-optic sensors, *J. Lightwave Technol.,* **13**: 1193–1199, 1995.
11. D. Dongalic and M. Zavrsnik, Fiber-optic microbend sensor structure, *Opt. Lett.,* **22**: 837–839, 1997.
12. W. B. Spillman and J. R. Lord, Self-referencing multiplexing technique for intensity modulating sensors, *Proc. SPIE,* **718**: 182–191, 1987.
13. J. W. Berthold et al., Design and characterization of a high temperature pressure transducer, *J. Lightwave Technol.,* **5**: 870–876, 1987.
14. B. G. Grossman et al., Fiber optic pore pressure sensor development, *Transportation Res. Rec.,* **1432**: 76–85, 1994.
15. O. Lumholt et al., Simple low-temperature sensor that uses microbending loss, *Opt. Lett.,* **16**: 1355–1357, 1991.
16. J. B. Freal, C. J. Zarobila, and C. M. Davis, A microbend horizontal accelerometer for borehole deployment, *J. Lightwave Technol.,* **5**: 993–996, 1987.
17. J. D. Weiss, Strain gage, *J. Lightwave Technol.,* **7**: 1308–1318, 1989.
18. D. Varshneya, J. L. Maida, and M. A. Overstreet, Speed sensor for advanced gas turbine engine control, *Proc. SPIE,* **1367**: 181–191, 1991.
19. P. Raatikainen et al., Fiber-optic liquid-level sensor, *Sensors Actuators,* **A58**: 93–97, 1997.
20. G. Betta, A. Pietrosanto, and A. Scaglione, A digital liquid level transducer based on optical fiber, *IEEE Trans. Instrum. Meas.* **45**: 551–555, 1996.
21. W. J. Bock, M. Beaulieu, and A. Domanski, GaAs-based fiber-optic pressure sensor, *IEEE Trans. Instrum. Meas.* **41**: 68–71, 1992.
22. Nortech Fibronic Inc., Québec, Canada, 1997, Catalog.
23. B. Culshaw, J. Foley, and I. P. Giles, A balancing technique for optical fiber intensity modulated transducers, *Proc. SPIE,* **574**: 117–120, 1984.
24. W. J. Bock and T. A. Eftimov, Single- and few mode fiber-optic pressure sensors, in F. Ansari (ed.), *Application of Fiber-Optic Sensors in Engineering Mechanics,* New York: American Society of Civil Engineers, 1993, pp. 252–263.

25. T. A. Eftimov, Resultant mode pattern and polarization in a LP_{01}, LP_{02} two-mode linearly birefringent optical fibre, *Opt. Quantum Electron.,* **23**: 1143–1160, 1991.

26. A. W. Snyder and J. D. Love, *Optical Waveguide Theory,* London: Chapman and Hall, 1983.

27. W. J. Bock and T. R. Wolinski, Temperature-compensated strain sensor based on polarization-rotated reflection, *Proc. SPIE,* **1370**: 189–196, 1991.

28. W. J. Bock et al., Cross-sensitivity effect in temperature compensated sensors based on highly birefringent fibers, *Appl. Opt.,* **33**: 6078–6083, 1994.

29. G. W. Day, K. B. Rochford, and A. H. Rose, Fundamentals and problems of fiber current sensors, *Proc. Int. Conf. Optical Fiber Sensors OFS-11,* Japan Society of Applied Physics, Sapporo, Japan, 1996, pp. 124–129.

30. G. W. Day and A. H. Rose, Faraday effect sensors: The state of the art, *Proc. SPIE,* **985**: 138–151, 1988.

31. M. Willsch, T. Bosselmann, and M. Bretschneider, Investigation of the vibration sensitivity of different annealed fiber optic current transformers, *Proc. Int. Conf. Optical Fiber Sensors OFS-12,* Williamsburg, VA, Optical Society of America, 1997, pp. 642–645.

32. J. E. Lenz, C. D. Anderson, and L. K. Strandjord, Magnetic materials characterization using a fiber optic magnetometer, *J. Appl. Phys.,* **57**: 3820–3822, 1985.

33. M. Ko and E. Garmire, Current sensing using bismuth rare-earth iron garnet films, *Appl. Opt.,* **34**: 1692–1696, 1995.

34. N. Inoue and K. Yamasawa, Stabilization of temperature dependence of Verdet constant of Bi-doped garnet and development of high sensitive optical fiber magnetic field sensor, *Electr. Eng. Jpn,* **117**: 1–10, 1996.

35. P. I. Nikitin et al., Fiber-optical magnetic field sensors based on Faraday effect in new materials, *Proc. SPIE,* **1584**: 124–134, 1992.

36. T. Valis, D. Hogg, and R. Measures, Fiber-optic Fabry–Perot strain gauge, *IEEE Photonics Technol. Lett.,* **2**: 227–228, 1990.

37. T. W. Kao and H. F. Taylor, High-sensitivity intrinsic fiber-optic Fabry–Perot pressure sensor, *Opt. Lett.,* **21**: 615–617, 1996.

38. T. Liu et al., Simultaneous strain and temperature measurement using a combined fiber Bragg grating/extrinsic Fabry–Perot sensor, *Proc. Int. Conf. Optical Fiber Sensors OFS-12,* Williamsburg, VA, OSA, 1997, pp. 40–43.

39. T. S. Priest, G. B. Scelsi, and G. A. Woolsey, Optical fiber sensor for electric field and electric charge using low-coherence, Fabry–Perot interferometry, *Appl. Opt.,* **36**: 4505–4508, 1997.

40. M. Born and E. Wolf, *Principles of Optics,* Oxford: Pergamon, 1986.

41. P. C. Beard and T. N. Mills, Extrinsic optical-fiber ultrasound sensor using a thin polymer film as a low-finesse Fabry–Perot interferometer, *Appl. Opt.,* **35**: 663–675, 1996.

42. K. A. Murphy et al., Quadrature phase-shifted, extrinsic Fabry–Perot optical fiber sensors, *Opt. Lett.,* **16**: 273–275, 1991.

43. N. Fürstenau and M. Schmidt, Fiber-optic extrinsic Fabry–Perot interferometer vibration sensor with two-wavelength passive quadrature readout, *IEEE Trans. Instrum. Meas.,* **47**: to be published.

44. G. Boheim, Fiber-linked interferometric pressure sensor, *Rev. Sci. Instrum.,* **58**: 1655–1659, 1987.

45. Y.-J. Rao and D. A. Jackson, Recent progress in fiber optic low-coherence interferometry, *Meas. Sci. Technol.,* **7**: 981–999, 1996.

46. H.-S. Choi and H. F. Taylor, High performance fiber optic temperature sensor using low-coherence interferometry, *Proc. Int. Conf. Optical Fiber Sensors OFS-12,* Williamsburg, VA, OSA, 1997, pp. 570–573.

47. S. Chen, A. J. Rogers, and B. T. Meggitt, Electronically scanned optical-fiber Young's white-light interferometer, *Opt. Lett.,* **16**: 761–763, 1991.

48. Y.-J. Rao and D. A. Jackson, Prototype fiber-optic-based ultrahigh pressure remote sensor with built-in temperature compensation, *Rev. Sci. Instrum.,* **65**: 1695–1698, 1994.

49. R. Dandliker, E. Zimmermann, and G. Frosio, Noise-resistant signal processing for electronically scanned white-light interferometry, *Proc. Int. Conf. Optical Fiber Sensors OFS-8,* Monterey, CA, OSA, 1992, pp. 53–56.

50. W. J. Bock, W. Urbanczyk, and M. B. Zaremba, Electronically scanned white-light interferometric strain sensor employing HB fibers, *Opt. Commun.,* **101**: 157–162, 1993.

51. W. J. Bock et al., White-light interferometric fiber-optic pressure sensor, *IEEE Trans. Instrum. Meas.,* **44**: 694–697, 1995.

52. G. Meltz, Overview of fiber grating-based sensors, *Proc. SPIE,* **2838**: 2–22, 1996.

53. H. Kogelnik, Theory of dielectric waveguides, in T. Tamir (ed.), *Integrated Optics,* Berlin: Springer-Verlag, 1979, pp. 66–79.

54. P. Ferdinand et al., Applications of Bragg grating sensors in Europe, *Proc. Int. Conf. Optical Fiber Sensors OFS-12,* Williamsburg, VA, OSA, 1997, pp. 14–19.

55. J. D. C. Jones, Review of fiber sensor techniques for temperature-strain discrimination, *Proc. Int. Conf. Optical Fiber Sensors OFS-12,* Williamsburg, VA, OSA, 1997, pp. 36–39.

56. G. A. Sanders et al., Progress in high performance fiber optic gyros, *Proc. Int. Conf. Optical Fiber Sensors OFS-12,* Williamsburg, VA, OSA, 1997, pp. 116–121.

57. J. P. Dakin (ed.), *The Distributed Fiber Optic Sensing Handbook,* Berlin: Springer-Verlag, 1990.

58. A. H. Hartog, A distributed temperature sensor based on liquid-core optical fibers, *J. Lightwave Technol.,* **1**: 498–509, 1983.

59. M. Tsubokawa, T. Higashi, and Y. Negishi, Mode couplings due to external forces distributed along a polarization maintaining fiber: An evaluation, *Appl. Opt.,* **27**: 166–173, 1988.

60. T. R. Parker et al., Temperature and strain dependence of the power level and frequency of spontaneous Brillouin scattering in optical fibers, *Opt. Lett.,* **22**: 787–789, 1997.

61. T. Horiguchi et al., Development of a distributed sensing technique using Brillouin scattering, *J. Lightwave Technol.,* **13**: 1296–1302, 1995.

62. M. Fahadirousan and R. C. Youngquist, Polarimetric coherence multiplexing using high-birefringence optical-fiber sensors, *Opt. Lett.,* **15**: 786–888, 1990.

63. B. D. Zimmermann et al., Fiber-optic sensors using high-resolution optical time domain instrumentation systems, *J. Lightwave Technol.,* **8**: 1273–1277, 1990.

64. J. Castracane and L. P. Clow, 64 channel fiber optic spectrometer for a dual wavelength interferometric pressure sensor array, *Rev. Sci. Instrum.,* **66**: 3668–3671, 1995.

65. C. Meunier et al., Industrial prototype of a fiber-optic sensor network for the thermal monitoring of the turbogenerator of a nuclear power plant—design, qualification and settlement, *J. Lightwave Technol.,* **13**: 1354–1361, 1995.

66. E. Bois, R. C. Spooncer, and B. E. Jones, A hybrid resonant differential pressure transmitter with wavelength-multiplexed power and data channels, in H. J. Arditty, J. P. Dakin, and R. T. Kersten (eds.), *Optical Fiber Sensors,* Springer Proceedings in Physics 44, New York: Springer-Verlag, 1989, pp. 478–483.

67. K. Fritsh, G. Beheim, and J. Sotomajor, Digital angular position sensor using wavelength division multiplexing, *Proc. SPIE,* **1169**: 453–460, 1989.

68. B. Deboux et al., A time division multiplexed multiwavelength optical fibver pH sensor, *Proc. Int. Conf. Optical Fiber Sensors OFS-11,* Sapporo, Japan, 1996, pp. 466–469.
69. S. Koto et al., Multipoint sensing laser Doppler velocimetry based on laser diode frequency modulation, *Proc. Int. Conf. Optical Fiber Sensors OFS-11,* Sapporo, Japan, 1996, pp. 606–609.
70. J. Mlodzianowski, D. Uttamchandani, and B. Culshaw, A simple frequency domain multiplexing system for optical point sensors, *J. Lightwave Technol.,* **5**: 1002–1007, 1987.
71. R. H. Wentworth, Theoretical noise performance of coherence-multiplexed interferometric sensors, *J. Lightwave Technol.,* **7**: 941–956, 1989.
72. W. J. Bock and W. Urbanczyk, Multiplexing of white-light interferometric fiber-optic sensors for hydrostatic pressure and temperature measurements, *Proc. Int. Conf. Optical Fiber Sensors OFS-12,* Williamsburg, VA, OSA, 1997, pp. 479–483.
73. W. J. Bock, W. Urbanczyk, and M. R. H. Voet, Performance and application of fiber-optic pressure cell for direct stress measurements, *Proc. Canadian Inst. Mining Conf.,* Edmonton, Canada, 1996, CD ed.
74. M. Lequime et al., A dual wavelength passive homodyne detection unit for fiber coupled white light interferometers, *Proc. SPIE,* **1267**: 288–293, 1990.
75. M. Wlodarczyk and G. He, A fiber-optic combustion pressure sensor system for automotive engine control, *Sensors,* **11**: 35–42, 1994.
76. T. Nishimoto et al., Development of 66 kV XLPE submarine cable using optical fiber as a mechanical-damage-detection-sensor, *IEEE Trans. Power Delivery,* **10**: 1711–1717, 1995.
77. N. Fürstenau et al., Extrinsic Fabry–Perot interferometer vibration and accoustic sensor systems for airport ground traffic monitoring, *IEE Proc. Optoelectron.,* **144**: 134–144, 1997.
78. H. Kajioka et al., Mass-produced I-FOGs for commercial applications, *Proc. Int. Conf. Optical Fiber Sensors OFS-11,* Sapporo, Japan, 1996, pp. 68–71.
79. D. Inaudi, Field testing and application of fiber-optic displacement sensors in civil structures, *Proc. Int. Conf. Optical Fiber Sensors OFS-12,* Williamsburg, VA, OSA, 1997, pp. 596–599.
80. D. Inaudi et al., Low-coherence deformation sensors for the monitoring of civil-engineering structures, *Sensors and Actuators,* **A44**: 125–130, 1994.
81. N. Itoh et al., Commercial current sensor activity in Japan, *Proc. Int. Conf. Optical Fiber Sensors OFS-12,* Williamsburg, VA, OSA, 1997, pp. 92–95.

WOJTEK J. BOCK
Université du Québec à Hull
MIROSLAW A. KARPIERZ
Warsaw University of Technology

FIELD EFFECT TRANSISTOR, JUNCTION GATED.

See JUNCTION GATE FIELD EFFECT TRANSISTORS.

FIELD EFFECT TRANSISTOR LOGIC CIRCUITS.

See GALLIUM ARSENIDE FIELD EFFECT TRANSISTOR LOGIC CIRCUITS.